## nature structural & molecular biology

**Article** 

https://doi.org/10.1038/s41594-024-01379-3

## Structural insight into synergistic activation of human 3-methylcrotonyl-CoA carboxylase

Received: 21 October 2023

Accepted: 25 July 2024

Published online: 02 September 2024

Check for updates

Jiayue Su 16, Xuyang Tian<sup>1,6</sup>, Hang Cheng 16, Desheng Liu<sup>1,6</sup>, Ziyi Wang<sup>1</sup>, Shan Sun 1 Hong-Wei Wang 1 & Sen-Fang Sui 1 L

The enzymes 3-methylcrotonyl-coenzyme A (CoA) carboxylase (MCC), pyruvate carboxylase and propionyl-CoA carboxylase belong to the biotin-dependent carboxylase family located in mitochondria. They participate in various metabolic pathways in human such as amino acid metabolism and tricarboxylic acid cycle. Many human diseases are caused by mutations in those enzymes but their structures have not been fully resolved so far. Here we report an optimized purification strategy to obtain high-resolution structures of intact human endogenous MCC, propionyl-CoA carboxylase and pyruvate carboxylase in different conformational states. We also determine the structures of MCC bound to different substrates. Analysis of MCC structures in different states reveals the mechanism of the substrate-induced, multi-element synergistic activation of MCC. These results provide important insights into the catalytic mechanism of the biotin-dependent carboxylase family and are of great value for the development of new drugs for the treatment of related diseases.

The biotin-dependent carboxylase family includes acetyl-coenzyme A (ACoA) carboxylase, 3-methylcrotonyl-CoA (MCoA) carboxylase, propionyl-CoA carboxylase (PCC) and pyruvate carboxylase (PC) in humans<sup>1-6</sup>. Among them, MCC, PCC and PC locate in the mitochondrial matrix and participate in metabolism of amino acids, fatty acids, cholesterol and glucose<sup>7-18</sup>. MCC is responsible for the conversion of MCoA to 3-methylglutaconyl-CoA, the fourth step in the leucine catabolic pathway<sup>12,15,19,20</sup>. PCC catalyzes propionyl-CoA to methylmalonyl-CoA and its metabolites finally participate in the tricarboxylic acid cycle<sup>1,21-23</sup>. PC is crucial in metabolic pathways such as gluconeogenesis, lipogenesis, glycogen synthesis, glucose-induced insulin secretion and biosynthesis of the neurotransmitter glutamate through carboxylating pyruvate to oxaloacetate24-29.

The biotin-dependent carboxylases are normally composed of several components named the biotin carboxyl carrier protein (BCCP) domain, biotin carboxylase (BC) domain and carboxyltransferase (CT) domain<sup>30-35</sup>. There is also a domain mediating the BC and CT interaction called the BT domain in MCC and PCC. A unique domain called the PT domain is responsible for tetramerization in  $PC^{16,26,34,36-40}$ . The catalytic process mediated by the biotin-dependent carboxylase could be defined in two steps: first, the biotin covalently attached in BCCP is catalyzed by BC domain under the existing  $\rm Mg^{2+}$  and  $\rm ATP^{3,41}.$  In this reaction, bicarbonate offers the carboxyl group and transfers it to N1 atom on biotin. The BC domain provides the binding pocket for MgATP and bicarbonate 35,42,43. Second, the BCCP serves as a 'swinging domain' to move the carboxylated biotin to the CT domain, where the carboxyl group is transferred from the biotin to the substrate<sup>30,37</sup>.

In recent years, people have obtained many structures of MCC, PCC and PC from various species 16,36,44-52. In 2011, Huang et al. reported  $two\,structures\,of\,the\,MCC\,holoenzyme\,from \textit{Pseudomonas aeruginosa}$ 

State Key Laboratory of Membrane Biology, Beijing Frontier Research Center for Biological Structures, School of Life Sciences, Tsinghua University, Beijing, China. 2The California Institute for Quantitative Biosciences (QB3), University of California campuses at Berkeley, Berkeley, CA, USA. 3Ministry of Education Key Laboratory of Protein Sciences, School of Life Sciences, Tsinghua University, Beijing, China. 4Tsinghua-Peking Joint Center for Life Sciences, School of Life Sciences, Tsinghua University, Beijing, China. 5School of Life Sciences, Cryo-EM Center, Southern University of Science and Technology, Shenzhen, China. <sup>6</sup>These authors contributed equally: Jiayue Su, Xuyang Tian, Hang Cheng, Desheng Liu. 🖂 e-mail: shansun@mail.tsinghua.edu.cn; hongweiwang@tsinghua.edu.cn; suisf@mail.tsinghua.edu.cn

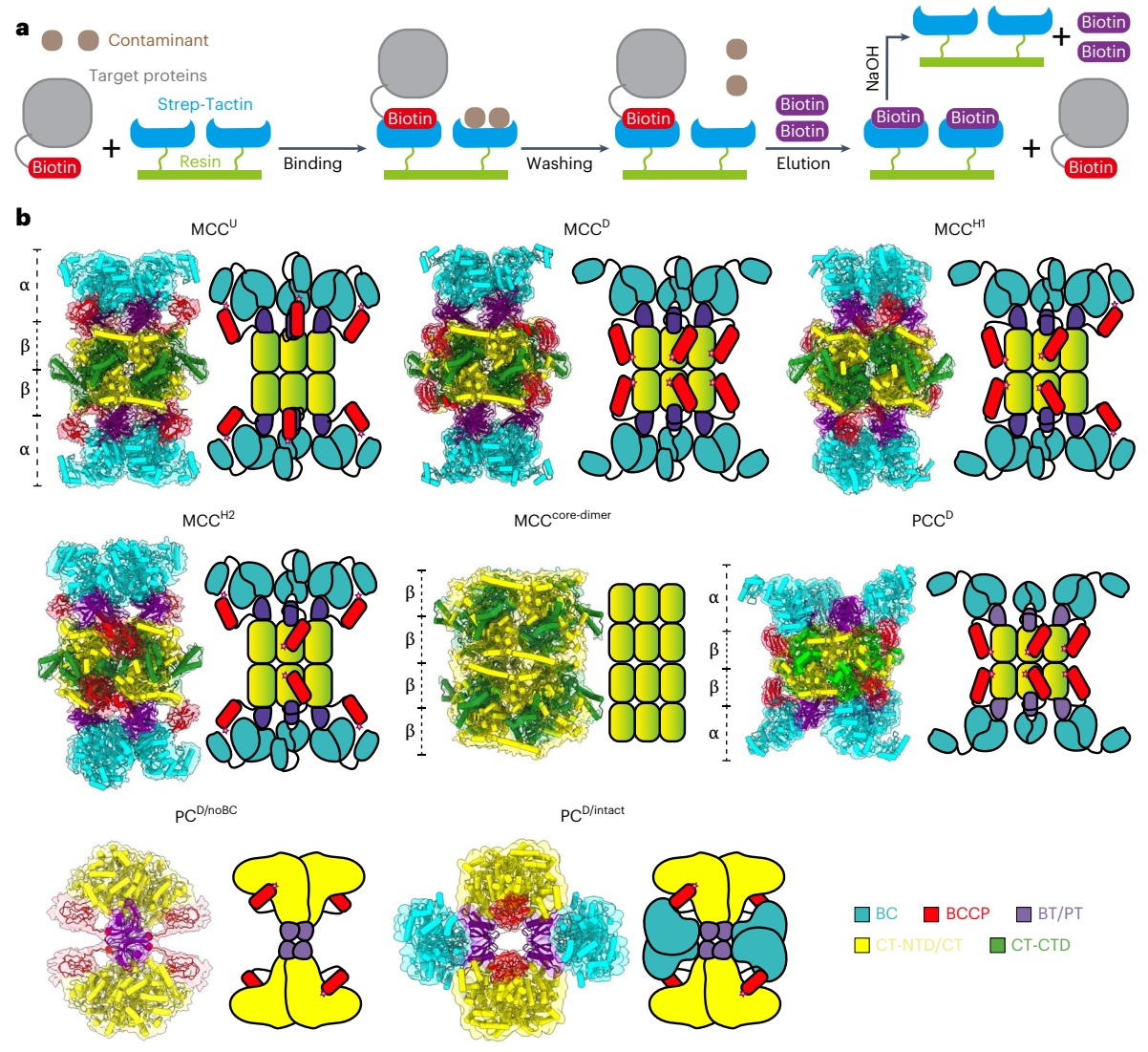


**Fig. 1**| **BAS** method and overall EM density maps. a, Schematic diagram for the mechanism of the biotin-binding protein purification by Strep-Tactin beads. b, Atomic models overlapped with density maps (displayed on the left) and structure diagrams (displayed on the right) of MCC<sup>U</sup>, MCC<sup>D</sup>, MCC<sup>HI</sup>, MCC<sup>HI</sup>,

 $MCC^{Core-Dimer}, PCC^D, PCD^{D/noBC} \ and \ PCD^{D/intact}. \ The \ BC \ domain \ is \ colored \ in \ cyan, the BCCP \ domain \ is \ colored \ in \ red, the \ BT \ and \ PT \ domain \ are \ colored \ in \ purple, the CT-NTD \ domain \ of \ MCC \ and \ PCC \ is \ colored \ in \ yellow, the \ CT \ domain \ of \ PC \ is \ also \ colored \ in \ yellow \ and \ the \ CT-CTD \ domain \ of \ MCC \ and \ PCC \ is \ colored \ in \ green.$ 

(PaMCC): one structure contains no BCCP domain, and the other structure contains only one BCCP domain after addition of the substrate MCoA that was modeled as CoA in the resolved structure<sup>36</sup>. In 2023, Lee et al. reported a MCC structure in the filament state from *Leish*mania tarentolae<sup>44</sup>. For PCC, Diacovich et al. reported the structure of PCCβ hexamer from *Streptomyces coelicolor* (ScPCCβ) bound to the substrate propionyl-CoA (PCoA) in 2004<sup>45</sup>. After that, the chimera PCC holoenzyme (Rp-RdPCC) structure containing α-subunit from Ruegeria pomeroyi PCC and β-subunit from Roseobacter denitrificans PCC was resolved by Huang et al. in 2010<sup>16</sup>. In 2021, Scheffen et al. resolved the structure of the Methylorubrum extorquens PCC (MePCC) incubated with glycolyl-CoA that was modeled as CoA in the final model<sup>46</sup>. It should be noted that all these structures are in a state where BCCP is bound to the CT domain. In 2022, Chai et al. determined a series structure of the human PC in different states including the state of BCCP binding to BC, but the resolution of this state was very low<sup>47</sup>. Therefore, although the two-step reaction of biotin-dependent carboxylase has been widely recognized, the lack of the high-resolution structures in the first reaction state makes it difficult to discover the conformational changes from the first to the second reaction step, which is necessary

to understand the molecular mechanism of the biotin-dependent carboxylase. To address those questions, we optimized a method for purifying endogenous biotin-dependent proteins without any gene modification from human embryonic kidney (HEK) 293F cells and obtained eight structures of MCC, PCC and PC complexes in different conformational states. Together with the structures of MCC bound to different substrates, we provided important insights into the reaction mechanism.

## Purifying human endogenous biotin-dependent carboxylases

By using the principle of the high affinity and specificity of the interaction of biotin with the egg-white glycoprotein avidin and with the related bacterial protein streptavidin, biotinylated proteins can be purified using avidin or streptavidin-coated resins<sup>53</sup>. Biotin-dependent carboxylases need to be covalently bonded to biotin to exert its physiological activity<sup>16</sup> and thus they can specifically bind to avidin or streptavidin resins. Using reversible binding of the biotinylated proteins to monovalent avidin, biotinylated PCs have been purified from chicken liver, sheep liver, pig liver and so on in the 1960s and 1970s<sup>54-56</sup>. In this

work, we also applied this avidin and streptavidin affinity principle to purify the human endogenous biotin-dependent carboxylases by using the commercially available Strep-Tactin affinity resins, and named this method biotin-affinity strep (BAS) (Fig. 1a). According to the manufacturer, the binding affinity of biotin to Strep-Tactin is not as high as for streptavidin and, therefore, biotinylated proteins can bind to Strep-Tactin in a reversible manner. The binding is released under mild and physiological conditions by adding an excess of free biotin (https://www.iba-lifesciences.com/media/09/9b/36/1705480836/Protocol\_BioID.pdf).

In this method, we first isolated mitochondria from HEK293F cells to reduce the effect of cytoplasmic proteins on purification. Then the mitochondria were broken and the lysate was incubated with the Strep-Tactin affinity resins directly. After washing, proteins were eluted from resins by competing with high concentration of biotin, and examined by Coomassie blue staining of sodium dodecyl sulfate-polyacrylamide gel electrophoresis (SDS-PAGE) gels. MCCα, MCCβ, PCCα, PCCβ and PC were obtained at -81, 61, 80, 58 and 130 kDa, respectively, and further confirmed by mass spectrometry (Extended Data Figs. 1–3 and Supplementary Tables 1 and 2). These results indicate that we have successfully obtained high-purity human endogenous MCC, PCC and PC from the mitochondria using the BAS method. In this way, the protein complex is extracted directly from the cell in the native state, which avoids cellular stress caused by gene overexpression or modification, and therefore may maintain its natural functional conformations, while overexpressed protein may misfold and leave the protein in a nonfunctional state. We further used single-particle cryogenic-electron microscopy (cryo-EM) to resolve the structures of these complexes. Owing to the strong capacity of three-dimensional (3D) classification in dealing with structural heterogeneity, we were able to obtain seven structures using cryo-EM data collected from just one grid. These structures contain five different states of MCC and two different states of PC, and among them five conformations are at near-atomic resolution (Fig. 1b and Extended Data Fig. 1). We also determined one structure of intact PCC (Fig. 1b and Extended Data Fig. 2). These results demonstrate that the BAS method can not only isolate endogenous protein complexes with high purity, but can also capture the multiple conformational states of the complexes.

## Overall structures of MCC, PCC and PC in different states

The holoenzyme of human MCC is an 850 kDa hetero-dodecamer consisting of six  $\alpha$ -subunits and six  $\beta$ -subunits. The  $\alpha$ -subunit is composed of a BC domain, BT domain and BCCP domain, and the β-subunit is the CT domain. All subunits are assembled into four layers and each of the two outer layers contains three α-subunits. In particular, two central layers, each containing three β-subunits, assemble into a hexamer, forming the central core of the holoenzymes. We determined four reconstructions of MCC holoenzyme, referred to as  $MCC^{U}$ ,  $MCC^{D}$ ,  $MCC^{H1}$ and MCCH2, at resolutions of 2.52, 2.51, 2.70 and 3.88 Å, respectively (Fig. 1b, Table 1 and Extended Data Fig. 3). We also captured a state of two core hexamers stacked together (MCC<sup>Core-Dimer</sup>) at 4.16 Å, which may be related to the assembly of the MCC complex (Fig. 1b). Each reconstruction of MCC holoenzyme represents a different conformational state. While the organization of BC domains, BT domains and CT domains is very similar among the four states, the positions of BCCP domains are different. Two BCCP positions are observed. One is the BCCP domain binding to the BC domain (BCCP-BC state), the other one is the BCCP domain binding to the CT domain (BCCP-CT state). All BCCP domains are in a BCCP-BC state in MCC<sup>U</sup>, whereas all BCCP domains are in a BCCP-CT state in MCC<sup>D</sup>. In MCC<sup>HI</sup> and MCC<sup>H2</sup>, BCCP domains are in hybrid states. Three BCCP domains of each outer layer show that one binds with BC domain and two bind with CT domains in MCC<sup>H1</sup>, while two bind with BC domains and one binds with CT domain in MCCH2. Both MCC<sup>H1</sup> and MCC<sup>H2</sup> exhibit a C2 symmetry. It should be noted that the BC domain in the BCCP-BC state has a better EM density than that in the BCCP-CT state, suggesting a more stable conformation of the BC domain caused by the association of the BCCP domain (Fig. 1b). When comparing the monomers (defined as the assembly containing one  $\alpha$ -subunit together with one  $\beta$ -subunit that contacts the BCCP domain of this  $\alpha$ -subunit) of all MCC holoenzyme dodecamers, the monomers in BCCP-CT state are well superimposed, and those in the BCCP-BC state are also very similar except for a small difference of a loop nearby the biotin-binding site in CT domains due to its flexibility (Fig. 2a,b). Thus, we will discuss the detailed structural differences between MCC and MCC as representatives of the four states of MCC holoenzyme later.

We also resolved the structure of the whole human endogenous PCC holoenzyme at 2.59 Å, in which all BCCP domains bind to CT domains (PCCD) (Fig. 1b, Table 1 and Extended Data Fig. 2). Similar to the architecture of MCC, the structure of human  $\alpha 6\beta 6$  PCC contains a central hexamer core composed of three pairs of dimeric β-subunits and three  $\alpha$ -subunit monomers at each side of the core (Fig. 1b). The BC domains of three  $\alpha$ -subunits at the same side interact with each other in MCC, but do not contact in PCC (Fig. 1b). Additionally, the BT domain and the BCCP domain of each  $\alpha$ -subunit bind to two adjacent CT domains in MCC, while they bind to the same CT domain in PCC (Fig. 1b). The biotin inserts itself into the binding pocket and its N-1 of the ureido ring connects with the main-chain carbonyl oxygen (C=O) of F397 in the C-terminal domain of CT (CT-CTD) through a potential hydrogen bond (H-bond) (Fig. 2c). This kind of interaction was also observed in the structures of Rp-RdPCC and MePCC (Extended Data Fig. 4a), suggesting its conservation in both bacteria and human.

With BAS method, we determined two different conformations of human endogenous PC complex, PCD/noBC and PCD/intact, at 3.83 and 5.63 Å, respectively (Fig. 1b and Table 1). PC is composed of the N-terminal BC domain, the C-terminal BCCP domain, the central CT domain and a unique PT domain separated by the CT domain. The holoenzyme of human PC complex is a 480 kDa homotetramer. In PC  $^{\text{D/noBC}}$ where BC domains are invisible, the loop connecting the BCCP domain and PT domain is resolved clearly, which reveals that BCCP domain contacts with the CT domain on the same subunit (Fig. 2d), rather than the CT domain on another subunit as previously reported<sup>46</sup>. Indeed, the conformation of PC with BCCP contacting CT on the same subunit was functionally observed 40. In PC D/intact, we resolved four stable BC domains (Fig. 1b), which is contrast to the recent report that high concentration of ACoA stabilizes a BC dimer at the one side of the PC tetrameric core. while the BC dimer at the other side maintains flexibility<sup>46</sup> (Figs. 1b and 2e). Notably, the number of particles used to construct PCDD/noBC and PC<sup>D/intact</sup> was almost the same, suggesting that both conformations do exist in natural cells. However, due to the low resolution, it is unclear how these conformations are regulated.

## Conformational changes associated with BCCP movement in MCC

For the convenience of analysis, we named one  $\alpha$ -subunit, its closed  $\beta$ -subunit and the neighboring  $\beta$ -subunit that contacts the BCCP domain of this  $\alpha$ -subunit as  $\alpha^a$ ,  $CT^a$  and  $CT^b$ , respectively. The  $\beta$ -subunit opposite to  $CT^b$  is  $CT^c$ . Three notable differences are observed between MCC<sup>U</sup> and MCC<sup>D</sup> (Fig. 3a). First, compared to BCCP-CT state, the BCCP domain in the BCCP-BC state swings 95° toward the neighboring  $CT^b$  domain around Ser638, which leads to a distance of 56 Å between biotin molecules in the two states (Fig. 3b). Along with this variation, the conformation of a long loop (Ile631-Gly655/BCCP), named a swing loop, linking the BCCP domain to the BT domain in MCC also changes. In MCC<sup>U</sup>, this loop is almost invisible. In MCC<sup>D</sup>, the residues from Val640 to Thr645 of the swing loop are shown as an  $\alpha$ -helix (H<sub>640-645</sub>) (Fig. 3b), and the main-chain C=O of Thr645 together with the side group of Gln646 that immediately follows H<sub>640-645</sub> forms H-bonds with the guanidinium group of Arg268 from the N-terminal domain (NTD) of the neighboring

Table 1 | Cryo-EM data collection, refinement and validation statistics of MCC, PCC and PC

| Structure   | Human MCC                                   |   |   |   |   |   | Hum                        | an PC                      |
|---|---|---|---|---|---|---|----------------------------|----------------------------|
|   | D   | U<br>(EMD-36128)<br>(PDB 8JAK)              | H2<br>(EMD-36034)<br>(PDB 8J78)             | H1 (EMD-36038) (PDB 8J7D)                   | Core-Dimer<br>(EMD-36024)<br>(PDB 8J73) | (EMD <u>-</u> 33729)<br>(PDB 7YBU)          | D/noBC                     | D/intact                   |
|   | (EMD-36136)<br>(PDB 8JAW)                   |   |   |   |   |   | (EMD-36044)<br>(PDB 8J7O)  | (EMD-35059)<br>(PDB 8HWL)  |
| Data collection and p                               | processing                                  |   |   |   |   |   |                            |                            |
| Magnification                                       | 81,000                                      | 81,000                                      | 81,000                                      | 81,000                                      | 81,000                                  | 81,000                                      | 81,000                     | 81,000                     |
| Voltage (kV)  | 300   | 300   | 300   | 300   | 300                                     | 300   | 300                        | 300                        |
| Electron exposure (e <sup>-</sup> /Å <sup>2</sup> ) | 50  | 50  | 50  | 50  | 50                                      | 50  | 50                         | 50                         |
| Defocus range (µm)                                  | -1.3 to -1.8                                | -1.3 to -1.8                                | -1.3 to -1.8                                | -1.3 to -1.8                                | -1.3 to -1.8                            | -1.3 to -1.8                                | -1.3 to -1.8               | -1.3 to -1.8               |
| Pixel size (Å)                                      | 1.0979                                      | 1.0979                                      | 1.0979                                      | 1.0979                                      | 1.0979                                  | 1.0979                                      | 1.0979                     | 1.0979                     |
| Symmetry imposed                                    | D3  | D3  | C2  | C2  | D3                                      | D3  | D2                         | D2                         |
| Initial particle<br>images (no.)                    | 422,660                                     | 422,660                                     | 422,660                                     | 422,660                                     | 422,660                                 | 516.854                                     | 60,113                     | 60,113                     |
| Final particle<br>images (no.)                      | 53,474                                      | 63.281                                      | 10,701                                      | 53,820                                      | 1,474                                   | 83.375                                      | 21,326                     | 21,450                     |
| Map resolution (Å)                                  | 2.51  | 2.52  | 3.88  | 2.70  | 4.16                                    | 2.59  | 3.83                       | 5.63                       |
| FSC threshold                                       | 0.143                                       | 0.143                                       | 0.143                                       | 0.143                                       | 0.143                                   | 0.143                                       | 0.143                      | 0.143                      |
| Map resolution range (Å)                            | 2.0-4.0                                     | 2.0-4.0                                     | 3.0-7.0                                     | 2.0-4.0                                     | 3.0-7.0                                 | 2.0-4.0                                     | 3.0-7.0                    | 4.0-8.0                    |
| Refinement  |   |   |   |   |   |   |                            |                            |
| Initial model used<br>(PDB code)                    | Alphafold:<br>AF-Q96RQ3-F1,<br>AF-Q9HCC0-F1 | Alphafold:<br>AF-Q96RQ3-F1,<br>AF-Q9HCC0-F1 | Alphafold:<br>AF-Q96RQ3-F1,<br>AF-Q9HCC0-F1 | Alphafold:<br>AF-Q96RQ3-F1,<br>AF-Q9HCC0-F1 | Alphafold:<br>AF-Q9HCCO-F1              | Alphafold:<br>AF-P05165-F1,<br>AF-P05166-F1 | Alphafold:<br>AF-P11498-F1 | Alphafold:<br>AF-P11498-F1 |
| Map sharpening <i>B</i> factor (Ų)                  | 76.1  | 78.1  | 85.2  | 75.9  | 26.7                                    | 72.4  | 104.5                      | 407.5                      |
| Model composition                                   |   |   |   |   |   |   |                            |                            |
| Nonhydrogen<br>atoms                                | 55,404                                      | 55,668                                      | 55,018                                      | 55,522                                      | 55,242                                  | 54,318                                      | 21,168                     | 29,144                     |
| Protein residues                                    | 7,152                                       | 7,182                                       | 7,100                                       | 7,168                                       | 7,188                                   | 7,062                                       | 2,748                      | 3,764                      |
| Ligands   | 6   | 6   | 6   | 6   | 0                                       | 6   | 4                          | 4                          |
| B factors (Ų)                                       |   |   |   |   |   |   |                            |                            |
| Protein (mean)                                      | 88.11                                       | 86.25                                       | 86.55                                       | 87.57                                       | 77.66                                   | 81.41                                       | 93.57                      | 93.01                      |
| Ligand (mean)                                       | 45.86                                       | 45.86                                       | 45.86                                       | 45.86                                       | -                                       | 25.31                                       | 299.62                     | 299.62                     |
| R.m.s. deviations                                   |   |   |   |   |   |   |                            |                            |
| Bond lengths (Å)                                    | 0.016                                       | 0.019                                       | 0.020                                       | 0.014                                       | 0.013                                   | 0.008                                       | 0.014                      | 0.014                      |
| Bond angles (°)                                     | 1.412                                       | 1.687                                       | 1.821                                       | 1.436                                       | 1.234                                   | 1.272                                       | 2.077                      | 1.986                      |
| Validation  |   |   |   |   |   |   |                            |                            |
| MolProbity score                                    | 1.53  | 1.63  | 1.64  | 1.53  | 1.56                                    | 1.56  | 1.51                       | 1.44                       |
| Clashscore  | 10.35                                       | 9.77  | 10.69                                       | 10.10                                       | 10.91                                   | 10.69                                       | 9.62                       | 8.16                       |
| Rotamer outliers<br>(%)                             | 0.22  | 0.73  | 0.57  | 0.44  | 0.17                                    | 0.00  | 0.09                       | 0.13                       |
| Ramachandran plot                                   |   |   |   |   |   |   |                            |                            |
| Favored (%)   | 98.13                                       | 97.43                                       | 97.56                                       | 97.96                                       | 98.31                                   | 97.97                                       | 98.54                      | 98.61                      |
|   |   |   |   |   |   |   |                            |                            |
| Allowed (%)   | 1.87  | 2.41  | 2.27  | 2.04  | 1.61                                    | 2.03  | 1.46                       | 1.39                       |

CT domain (CTa-NTD) (Fig. 3c). Notably, Arg268 is stabilized by Trp276/CTa-NTD and Phe350/CTb-CTD through two  $\pi$ -cation interactions (Fig. 3c). Sequence alignment indicates that Gln646/BCCP, Arg268/CT and Trp276/CT are conserved as hydrophilic, positively charged and aromatic amino acids, respectively, among different species (Extended Data Fig. 5). In addition, strong hydrophobic interaction exists at the C terminal of the swing loop mediated by the completely conserved

Met653, Ala679 and Met680 from BCCP, and Phe377 and Met408 from CT $^b$ -CTD, as well as Val375/CT $^b$ -CTD that is also highly conserved as hydrophobic amino acid (Fig. 3c). Therefore, the conserved interactions between the swing loop and the surrounding CT domains are important for the positioning of the BCCP domain in the CT domain.

The second difference lies in a long loop (Gln402-Ala415/CT) near the biotin-binding site of the CT domain, named the biotin-binding loop

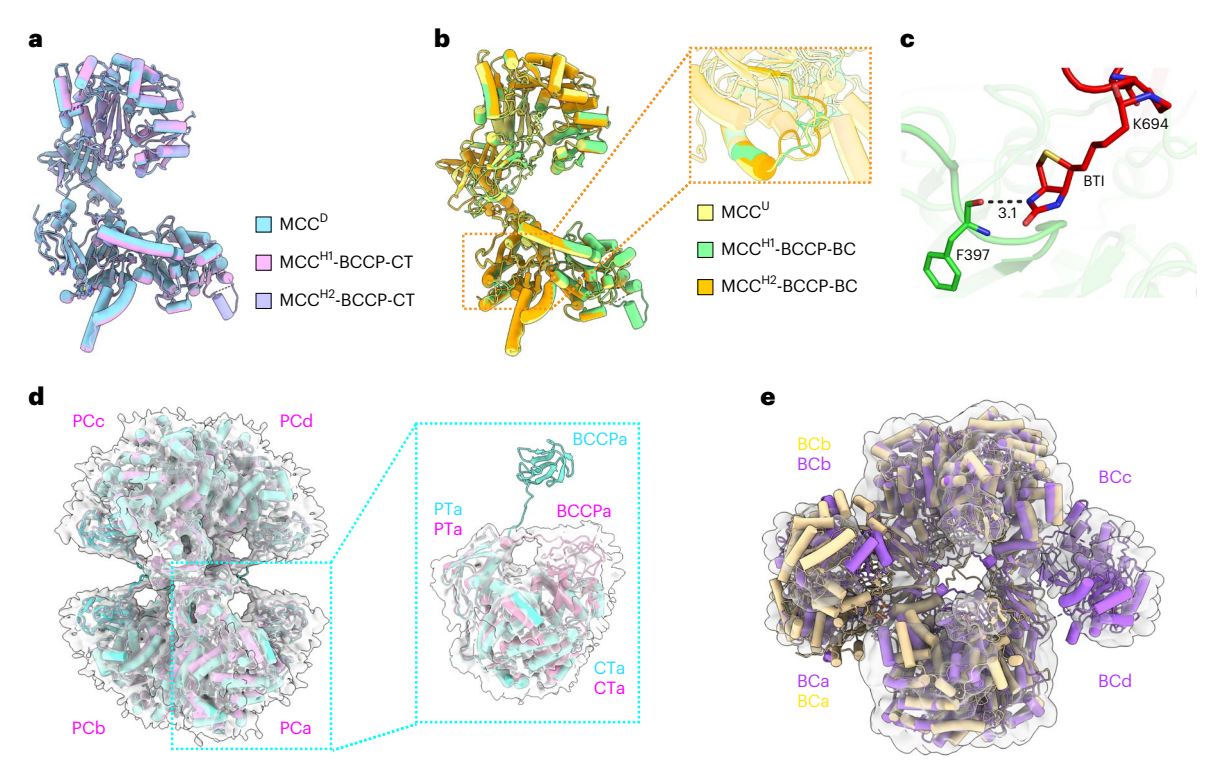


**Fig. 2** | **The details of MCC, PCC and PC. a**, Superimposition of monomers of BCCP-CT states from  $MCC^D$ ,  $MCC^{HI}$  and  $MCC^{H2}$ . **b**, Superimposition of monomers of BCCP-BC states from  $MCC^U$ ,  $MCC^{HI}$  and  $MCC^{H2}$ . The inset shows the diversity of the loop nearby the biotin-binding site in CT domains. **c**, The biotin interacts with F397 at the CT-CTD in PCC<sup>D</sup>. The potential H-bond is labeled by the black dashed line and the number indicates the distance (Å). **d**, The comparison of  $PC^{D/noBC}$  with previously reported human PC complex (PDB 7WTA) indicates that BCCP domain contacts with the CT domain on the same subunit, rather than CT domain on

another subunit as in PDB 7WTA. The inset shows the clear EM density of the loop linking BCCP and PT in PC $^{D/noBC}$ . PC $^{D/noBC}$  is colored in magenta and the reported PC structure is colored in cyan. **e**, The comparison of PC $^{D/intact}$  with the previously reported human PC complex (PDB 7WTC). In PC $^{D/intact}$ , four BC domains are stable, which is contrast to the recently reported PC complex (PDB 7WTC) where a high concentration of ACoA stabilizes a BC dimer at the one side of the PC tetrameric core, while the BC dimer at the other side maintains flexible  $^{47}$ . PC $^{D/intact}$  is colored in pink and the reported PC structure is colored in yellow.

(BB loop). Compared to  $MCC^U$  in which the BB loop is a fully extended loop, the residues from Arg411 to Ala415 of BB loop in  $MCC^D$  form an  $\alpha$ -helix (H<sub>411-415</sub>), which shortens BB loop and causes it to flip to the other side (Fig. 3d). Moreover, the BB loop itself in  $MCC^D$  has extensive interactions with biotin. The main-chain C=Os of Thr405 and Phe407 make H-bonds with the ureido ring of biotin, and a hydrophobic interaction occurs between Val375, Met408 and Val409 with biotin (Fig. 3e). These residues are also highly conserved across different species. Further structural analysis reveals that BB Loop in  $MCC^U$  seriously clashes with biotin in  $MCC^D$  state, thereby blocking biotin insertion (Fig. 3d). Together, the loop-to-helix conversion in BB loop and the movement of BB loop reshape the conformation of the biotin-binding pocket of CT, which is necessary for biotin stabilization.

The third difference is the presence of the region from Ala242 to Leu260 of the CT domain in MCC<sup>D</sup>, which is totally absent in MCC<sup>U</sup> (Fig. 3d). In MCC<sup>D</sup> state, this region, which consists of two intermediate  $\alpha$ -helices ( $H_{244-251}$  and  $H_{257-260}$ ) and the extended loops, is extensively linked with surrounding residues through both electrostatic and hydrophobic interactions. Lys248 and Glu253 from CT<sup>b</sup>-CTD formsalt bridges with Asp488 and Arg411 from CT<sup>b</sup>-CTD (Extended Data Fig. 6a). Two hydrophobic cores are formed by residue clusters of Ala242, Leu246, Val247 and Ala250 from CT<sup>c</sup>-NTD and Val409/CT<sup>b</sup>-CTD, and Phe240, Pro244, Val255 and Leu260 from CT<sup>c</sup>-NTD (Extended Data Fig. 6b). Sequence alignment indicates that these residues are all conserved in physico-chemical properties (Extended Data Fig. 4), suggesting a functional relevance of the stabilization of Ala242 to Leu260 of the CT domain in the MCC<sup>D</sup> state. Indeed, the completely conserved residues of Leu246, Ala249 and Ala250 from  $H_{244251}$  provide hydrophobic

interactions with biotin (Fig. 3f and Extended Data Fig. 5). When we take a closer look at the biotin-binding pocket, we find that in the absence of  $H_{244-251}$  there is a gap in this pocket (Fig. 3g), and  $H_{244-251}$  acts like a plug right blocking this gap (Fig. 3h). Therefore, a closed hydrophobic pocket is formed, allowing the biotin to be stable in this pocket (Fig. 3i). There is also a conflict between the BB loop in MCC<sup>U</sup> and  $H_{244-251}$  in MCC<sup>D</sup>, which may be the reason why the Ala242 to Leu260 region of the CT domain in the MCC<sup>U</sup> is flexible and thus invisible (Fig. 3d).

Taken together, the notable conformational changes between MCC and MCC , including the presence of the helix in the swing loop and BB loop, the flip of BB loop and the existence of  $H_{244-251}$ , are associated with the stabilization of biotin in the CT domain, which prepares the way for the next step of the carboxyl group transfer from the biotin to the substrate.

## Substrate binding induces biotin into the final active site

To further explore the mechanism of the enzymatic catalysis of substrate, we incubated the MCoA with MCC and determined the structures of the MCoA-binding MCC (MCC–MCoA) (Fig. 4 and Extended Data Fig. 7). Similar to the MCC in the apo form, MCC–MCoA also displays four different states, MCC–MCoA $^{\text{U}}$ , MCC–MCoA $^{\text{D}}$ , MCC–MCoA $^{\text{H}_{\text{I}}}$  and MCC–MCoA $^{\text{H}_{\text{I}}}$  with resolutions of 2.98, 2.81, 3.20 and 3.49 Å, respectively (Fig. 4a–d, Table 2 and Extended Data Fig. 7). The overall domain organizations of them are identical to their counterparts of MCC in the apo form, except the presence of the substrate MCoA. Because the samples with substrates were not crosslinked, the maps of MCC–MCoA show weaker densities for MCC $\alpha$  than those of MCC without substrates.

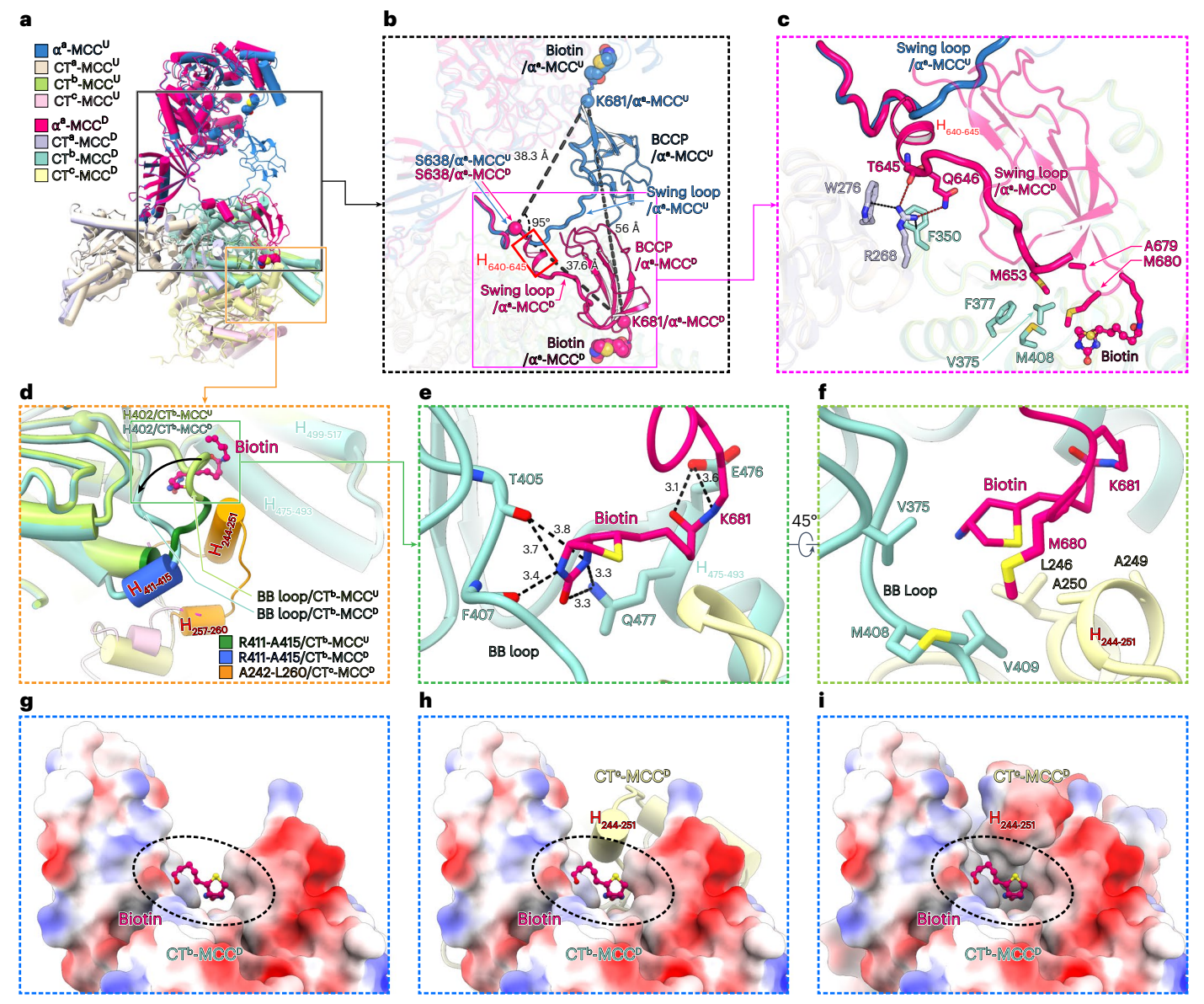


**Fig. 3** | **Conformational changes associated with the BCCP movement revealed by MCC structures in MCC<sup>U</sup> and MCC<sup>D</sup>. a**, Overall structural comparison of MCC<sup>U</sup> and MCC<sup>D</sup>. The domains are color coded. The subunits of  $\alpha^a$ , CT<sup>a</sup>, CT<sup>b</sup> and CT<sup>c</sup> of MCC<sup>U</sup> are colored in sky blue, wheat, limon and light pink, respectively. The subunits of  $\alpha^a$ , CT<sup>a</sup>, CT<sup>b</sup> and CT<sup>c</sup> of MCC<sup>D</sup> are colored in hot pink, light blue, green cyan and pale yellow, respectively. The regions boxed by black and orange lines are enlarged in **b** and **d**, respectively. **b**, Different positions and conformations of the swing loop (Ile631-Gly655) and biotin in MCC<sup>U</sup> and MCC<sup>D</sup>. The region boxed by magenta line is enlarged in **c. c**, Interactions between the swing loop and surrounding CT domains in MCC<sup>D</sup>. Potential H-bonds and the cation– $\pi$  interactions are labeled by red and black dashed lines, respectively.

**d**, Different positions and conformations of the BB loop (His402-Ala415) and the region of Ala242-Leu260. Two black triangles indicate the steric clashes between biotin/MCC<sup>D</sup> and BB loop/MCC<sup>U</sup>, and  $H_{244-251}$ /MCC<sup>D</sup> and BB Loop/MCC<sup>U</sup>. The regions of R411-A415 in CT<sup>D</sup> of MCC<sup>U</sup> and MCC<sup>D</sup> are colored in forest and deep blue, respectively. The region of A242-L260 in CT<sup>D</sup> of MCC<sup>D</sup> is colored in orange. The region boxed by green line is enlarged in **e. e.f.** Coordination of biotin in MCC<sup>D</sup> by both H-bonds (**e**) and hydrophobic interactions (**f**). Potential H-bonds are labeled with black dashed lines and the numbers near the lines indicate the distances (Å). **g-i**, The conformation of the biotin-binding pocket without  $H_{244-251}$  (**g**) and with  $H_{244-251}$  (**h,i**). CT<sup>D</sup>-MCC<sup>D</sup> is shown as an electrostatic surface.  $H_{244-251}$  is shown as a cartoon (**h**) or electrostatic surface (**i**).

The existence of both MCC–MCoA<sup>U</sup> and MCC–MCoA<sup>D</sup> with more particles of MCC–MCoA<sup>D</sup> than those of MCC–MCoA<sup>U</sup> (Extended Data Fig. 7) suggests that binding of substrate plays an essential role in stabilizing the biotin in the CT domain, but is not the determinate factor for biotin locating in the CT domain. Consistent with this observation, the position of the BB loop in MCC–MCoA<sup>U</sup> is similar to that in MCC<sup>U</sup>, which blocks the binding of the biotin to the CT domain (Fig. 5a). The most obvious difference between MCC<sup>U</sup> and MCC–MCoA<sup>U</sup> is the movement of one twisted hairpin composed of two successive  $\alpha$ -helices  $H_{475-493}$  and  $H_{499-517}$  from the CT domain (Fig. 5a), which is due to the MCoA

binding. The MCoA snuggles into the interface between two opposite CT domains  $CT^b$  and  $CT^c$  (Fig. 5a,b). The large conformational change of the two helices in the CT domain and the similar but different positions of the substrate were also observed in the crystal structure of PaMCC in complex with CoA (Extended Data Fig. 4b,c) $^{36}$ . In that work, MCoA was included in the crystallization solution, but only CoA was observed based on the electron density. However, the density of MCoA is clearly visible in our cryo-EM map (Extended Data Fig. 7l). The terminal dimethyl vinyl groups of MCoA are stabilized by the strong hydrophobic interactions with Phe185, Phe191 and Phe195 from  $CT^c$  as well as Tyr450

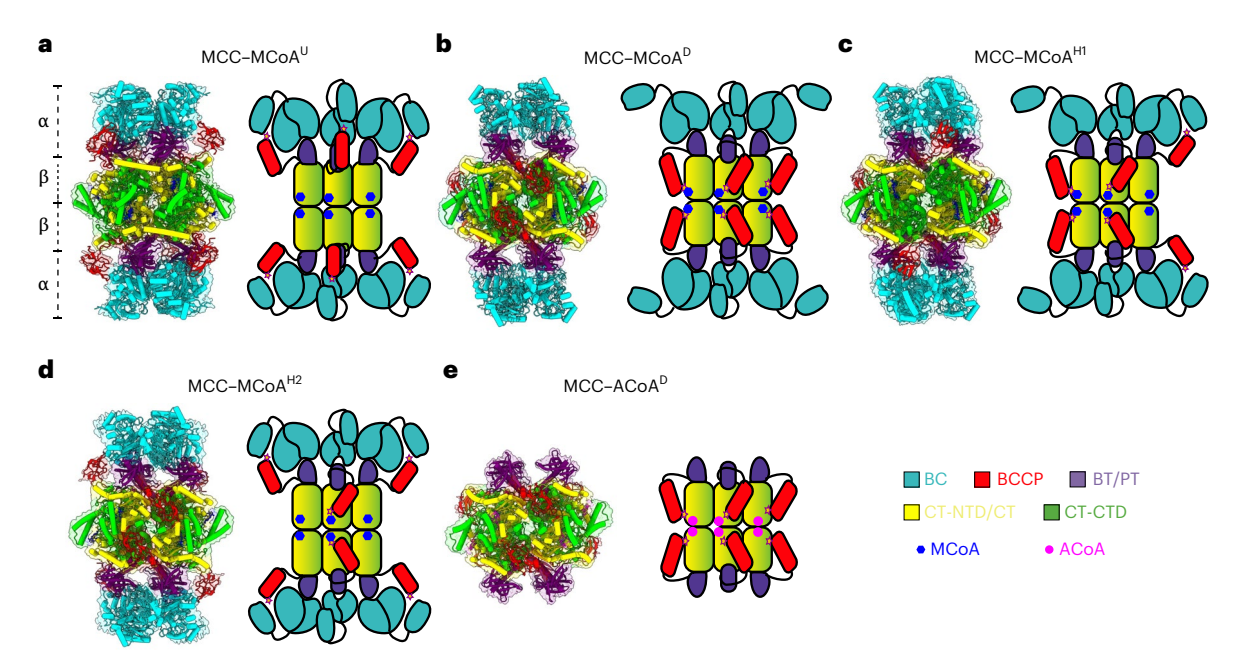


**Fig. 4** | **Overall EM density maps of substrate-bound MCC complexes. a**, Atomic model overlapped with a density map (displayed on the left) and structure diagram (displayed on the right) of MCC–MCoA $^{\text{U}}$ . **b**, Atomic model overlapped with a density map (displayed on the left) and structure diagram (displayed on the right) of MCC–MCoA $^{\text{D}}$ . **c**, Atomic model overlapped with

a density map (displayed on the left) and structure diagram (displayed on the right) of MCC–MCoA $^{\rm Hl}$ . **d**, Atomic model overlapped with a density map (displayed on the left) and structure diagram (displayed on the right) of MCC–MCoA $^{\rm H2}$ . **e**, Atomic model overlapped with a density map (displayed on the left) and structure diagrams (displayed on the right) of MCC–ACoA $^{\rm D}$ .

from CT<sup>b</sup> (Fig. 5b). Several potential H-bonds are formed between MCoA and backbones of residues Gly174, Ala176 and Leu178 from CT<sup>c</sup> (Fig. 5b). Tyr177 from CT<sup>c</sup> provides one parallel-displaced  $\pi$ - $\pi$  interaction with the adenine ring of MCoA (Fig. 5b). The phosphates of MCoA are surrounded by several positively charged or polar residues of Arg78 and Lys141 from CT<sup>c</sup> as well as Gln489 and Arg492 from CT<sup>b</sup> (Fig. 5b). Gln489 and Arg492 are located exactly in H<sub>475-493</sub>, so it can be concluded that their specific interactions with MCoA pull H<sub>475-493</sub> closer to MCoA, leading to a more compact conformation of the MCoA-binding pocket and thus stabilizing MCoA (Fig. 5b). The residues of Arg78, Lys141, Ala176 and F191 from CT<sup>c</sup> were also revealed to be involved in the CoA binding in the PaMCC-CoA complex 36.

Structural comparison of MCC-MCoA<sup>U</sup> and MCC-MCoA<sup>D</sup> shows that the positions of  $H_{475-493}$  and MCoA in them are almost the same (Fig. 5c,d), indicating that MCoA binding itself would be sufficient to induce the movement of H<sub>475-493</sub> and biotin binding has no effect on the binding and locating of MCoA. However, the position of biotin in CT domain of MCC<sup>D</sup> and MCC-MCoA<sup>D</sup> is close but different (Fig. 5d), suggesting that MCoA binding does affect the location of biotin. Compared to MCC<sup>D</sup>, the biotin in MCC-MCoA<sup>D</sup> penetrates further to the interface between CT<sup>b</sup> and CT<sup>c</sup>, and therefore is closer to MCoA (Fig. 5d). Consistent with the movement of biotin, the conformations of BCCP and H<sub>244-251</sub> also change (Fig. 5c). We named the biotin-binding pockets in MCC<sup>D</sup> and MCC-MCoA<sup>D</sup> as preactive and final active sites, respectively. Detailed analysis reveals that the shift of H<sub>475-493</sub> due to MCoA binding causes Glu476 and Gln477, which make extensive H-bonds with biotin in MCC<sup>D</sup>, to move away from biotin in MCC<sup>D</sup> (Fig. 5e). Thus, the H-bonds are broken and biotin escapes from the preactive site and relocates to the final active site. At the final active site, biotin is closely encompassed by a panel of hydrophobic residues including Phe407, Val409, Tyr445, Ala447 and Met473 from CTb, Ala218, Leu241, Ala242, Leu246 and Ala250 from CT<sup>c</sup>, and Met680 from BCCP (Fig. 5f). In addition, the backbones of Phe407 and Ala447 form potential H-bonds with the ureido ring of biotin (Fig. 5f). Among these residues, Phe407, Tyr445 and Met473 from CT<sup>b</sup> and Met680 from BCCP were also reported to enclose biotin in the PaMCC–CoA complex, in which the biotin is also located in the final active site (Extended Data Fig. 4c) $^{36}$ . We notice that the structures of PCC with and without propionyl-CoA also show two different positions of biotin $^{16,45,46}$ , which correspond to the final active site and the preactive site observed in MCC (Extended Data Fig. 4d). These results indicate that the existence of a preactive site and a final active site may be common in the biotin-dependent carboxylases and related to the reaction mechanism.

When we took a close look at the binding pockets of biotin and MCoA, it can be found that MCC<sup>D</sup> already has enough spaces to accommodate biotin in the final active site as well as MCoA (Fig. 5g,h). However, there is a steric hindrance between biotin in the final active site and CT<sup>b</sup> at the MCC<sup>D</sup> state, and the space is too large to hold MCoA firmly (Fig. 5h). Therefore, MCoA binding modifies the conformation of CT<sup>b</sup>, that is, H<sub>475-493</sub> moves toward MCoA, thus forming a more compact pocket that holds MCoA tightly (Fig. 5i). The change of H<sub>475-493</sub> could also reshape the conformation of the preactive site to release biotin and remove the steric clash to allow biotin into the final active site (Fig. 5i,j). At the final active site, biotin is trapped in the hydrophobic environment and is very close to MCoA, which is favorable for the next transfer of carboxyl group from biotin to MCoA (Fig. 5j).

To validate the importance of the final active site for the enzyme activity revealed by the structure, we generated two MCCβ mutants, L241R and A242F, and examined their enzyme activity (Extended Data Fig. 8). L241 and A242 provide hydrophobic environment for biotin stabilization in the final active site (Fig. 5f) and the mutations were designed to disrupt the biotin-binding pocket. The two mutants were purified and eluted at the same position from the size exclusion chromatography as the wild-type MCC, indicating that the mutations do not affect the holoenzyme formation (Extended Data Fig. 8a–d). For wild-type MCC, 12.6% of MCoA was retained after the addition of ATP, that is 87.4% of MCoA was carboxylated, which indicates high enzyme activity (Extended Data Fig. 8e,h). By contrast, for the two mutants, about 75% of MCoA was retained, that is -25% of MCoA was carboxylated, which indicates obviously reduced enzyme activity (Extended

Table 2 | Cryo-EM data collection, refinement and validation statistics of substrate-bound MCC

| Structure   | Human MCC                                   |   |   |   |   |  |  |
|---|---|---|---|---|---|--|--|
|   | MCoA <sup>u</sup>                           | MCoA <sup>D</sup>                           | MCoA <sup>H2</sup>                          | MCoA <sup>H1</sup>                          | ACoA <sup>D</sup>                           |  |  |
|   | (EMD-36704)<br>(PDB 8JXL)                   | (EMD-35980)<br>(PDB 8J4Z)                   | (EMD-36705)<br>(PDB 8JXM)                   | (EMD-36706)<br>(PDB 8JXN)                   | (EMD-36840)<br>(PDB 8K2V)                   |  |  |
| Data collection and processin                       | ıg  |   |   |   |   |  |  |
| Magnification                                       | 29,000                                      | 29,000                                      | 29,000                                      | 29,000                                      | 45,000                                      |  |  |
| Voltage (kV)  | 300   | 300   | 300   | 300   | 200   |  |  |
| Electron exposure (e <sup>-</sup> /Å <sup>2</sup> ) | 50  | 50  | 50  | 50  | 50  |  |  |
| Defocus range (µm)                                  | -1.5 to -1.8                                | −1.5 to −1.8                                | −1.5 to −1.8                                | −1.5 to −1.8                                | −1.5 to −1.8                                |  |  |
| Pixel size (Å)                                      | 0.97  | 0.97  | 0.97  | 0.97  | 0.94  |  |  |
| Symmetry imposed                                    | D3  | D3  | C2  | C2  | D3  |  |  |
| Initial particle images (no.)                       | 843.319                                     | 843.319                                     | 843.319                                     | 843.319                                     | 203,299                                     |  |  |
| Final particle images (no.)                         | 82,260                                      | 120,068                                     | 43,147                                      | 44,531                                      | 11,374                                      |  |  |
| Map resolution (Å)                                  | 2.98  | 2.81  | 3.49  | 3.20  | 3.52  |  |  |
| FSC threshold                                       | 0.143                                       | 0.143                                       | 0.143                                       | 0.143                                       | 0.143                                       |  |  |
| Map resolution range (Å)                            | 2.0-4.0                                     | 1.5-3.5                                     | 2.5-4.5                                     | 2.0-4.0                                     | 3.0-4.0                                     |  |  |
| Refinement  |   |   |   |   |   |  |  |
| Initial model used (PDB code)                       | Alphafold:<br>AF-Q96RQ3-F1,<br>AF-Q9HCCO-F1 | Alphafold:<br>AF-Q96RQ3-F1,<br>AF-Q9HCC0-F1 | Alphafold:<br>AF-Q96RQ3-F1,<br>AF-Q9HCC0-F1 | Alphafold:<br>AF-Q96RQ3-F1,<br>AF-Q9HCC0-F1 | Alphafold:<br>AF-Q96RQ3-F1,<br>AF-Q9HCC0-F1 |  |  |
| Map sharpening <i>B</i> factor (Ų)                  | 98.4  | 102.1                                       | 93.1  | 84.6  | 77.2  |  |  |
| Model composition                                   |   |   |   |   |   |  |  |
| Nonhydrogen atoms                                   | 30,581                                      | 53,664                                      | 55,018                                      | 55,522                                      | 35,202                                      |  |  |
| Protein residues                                    | 3,924                                       | 6,906                                       | 7,100                                       | 7,168                                       | 4,530                                       |  |  |
| Ligands   | 12  | 12  | 12  | 12  | 12  |  |  |
| B factors (Ų)                                       |   |   |   |   |   |  |  |
| Protein (mean)                                      | 156.36                                      | 206.75                                      | 86.55                                       | 87.57                                       | 173.42                                      |  |  |
| Ligand (mean)                                       | 128.56                                      | 122.41                                      | 45.86                                       | 45.86                                       | 180.15                                      |  |  |
| R.m.s. deviations                                   |   |   |   |   |   |  |  |
| Bond lengths (Å)                                    | 0.007                                       | 0.003                                       | 0.020                                       | 0.014                                       | 0.005                                       |  |  |
| Bond angles (°)                                     | 0.772                                       | 0.644                                       | 1.821                                       | 1.436                                       | 1.029                                       |  |  |
| Validation  |   |   |   |   |   |  |  |
| MolProbity score                                    | 1.69  | 1.78  | 1.64  | 1.53  | 1.99  |  |  |
| Clashscore  | 7.97  | 12.07                                       | 10.69                                       | 10.10                                       | 12.54                                       |  |  |
| Rotamer outliers (%)                                | 0.38  | 0.74  | 0.57  | 0.44  | 1.44  |  |  |
| Ramachandran plot                                   |   |   |   |   |   |  |  |
| Favored (%)   | 96.19                                       | 96.94                                       | 97.56                                       | 97.96                                       | 96.14                                       |  |  |
| Allowed (%)   | 3.81  | 3.06  | 2.27  | 2.04  | 3.86  |  |  |
| Disallowed (%)                                      | 0   | 0   | 0.17  | 0   | 0   |  |  |

 $Data\ Fig.\ 8f,g,h).\ These\ results\ further\ validate\ our\ structural\ findings\ that\ the\ final\ active\ site\ is\ necessary\ for\ MCC\ function.$ 

## Role of the preactive site in the substrate recognition

The determined structures show that there are two close but different positions of biotin in the CT domain: one far away from the substrate (the preactive site) and the other very close to the substrate (the final active site) (Fig. 5d). Then one question is why does biotin not go directly to the final active site when there is no substrate, but is in the preactive site? Because, if biotin enters the final active site directly, the catalytic reaction can be carried out immediately on substrate binding. If the biotin is standing by at the preactive site first, it will be necessary to

induce the further movement of biotin after substrate binding to start the reaction. Obviously, the latter approach is more time-consuming and energy-wasting. One possible explanation is that the existence of the preactive site plays a role in the substrate recognition.

To test the above hypothesis, we incubated MCC with ACoA, the specific substrate of ACoA carboxylase  $^{57}$ , and resolved the structure of this complex (MCC–ACoA $^{\rm D}$ ) (Fig. 4e, Table 2 and Extended Data Fig. 7). The structure shows that ACoA could bind to MCC in a position similar to, but slightly different from, MCoA, probably because the acetyl group is smaller than the methylcrotonyl group (Fig. 6a,b). ACoA binding also induces the movement of  $H_{475.493}$ , but to a lesser extent, as evidenced by the fact that the position of  $H_{475.493}$  in MCC–ACoA $^{\rm D}$  is between the position of this helix in MCC $^{\rm D}$  and MCC–MCoA $^{\rm D}$  (Fig. 6b).

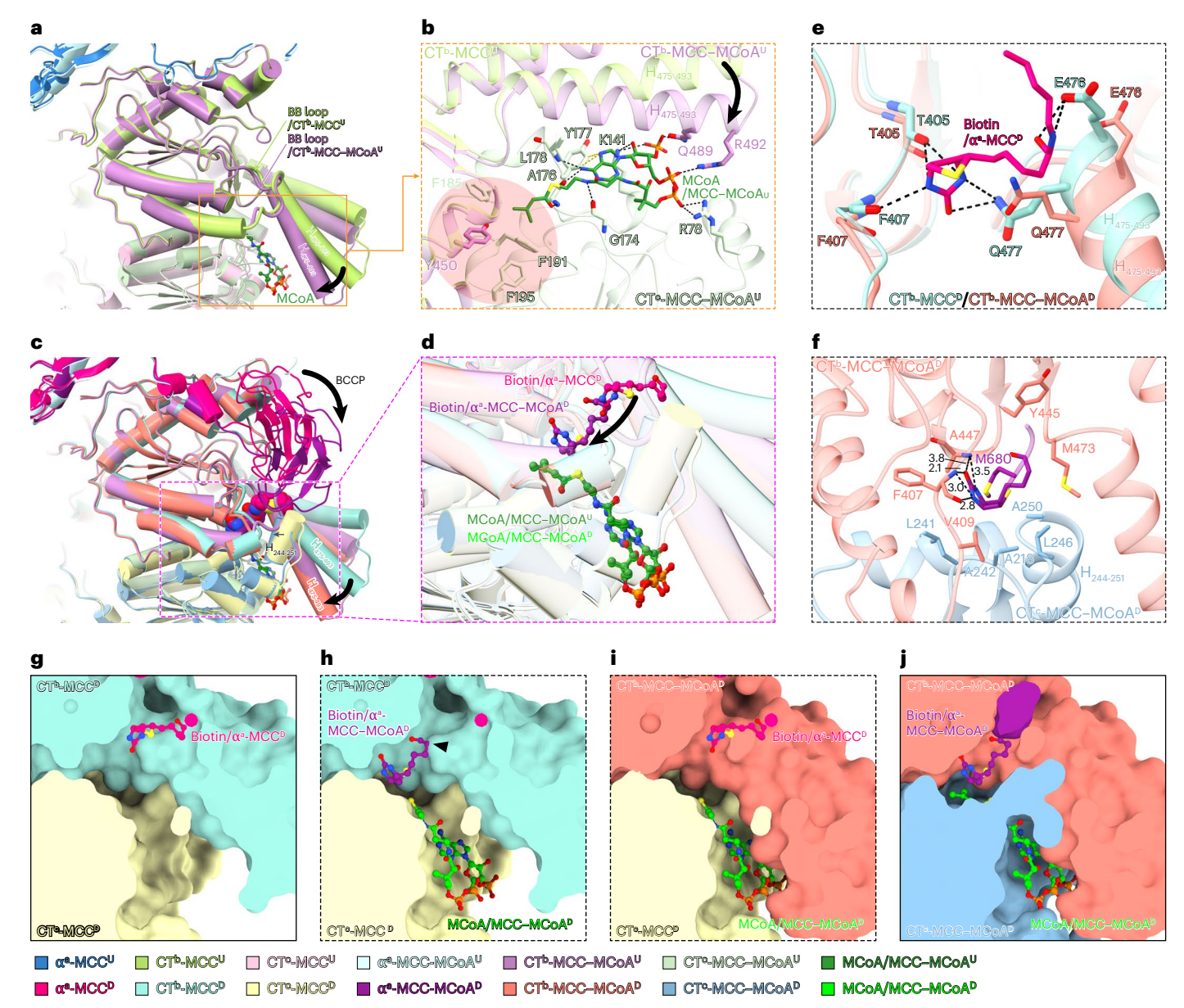


**Fig. 5** | **Binding of the substrate induces the biotin into the final active site. a**, Structural comparison of MCC<sup>U</sup> and MCC-MCoA<sup>U</sup>. The region boxed by orange line is enlarged in **b. b**, Coordination of MCoA in MCC-MCoA<sup>U</sup>. Potential H-bonds and the  $\pi$ - $\pi$  interaction are labeled by black and yellow dashed lines, respectively. **c**, Structural comparison of MCC<sup>D</sup>, MCC-MCoA<sup>D</sup> and MCC-MCoA<sup>U</sup>. The region boxed by magenta dashed line is enlarged in **d. d**, Close-up view of biotin and MCoA molecules in different states. **e**, The shift of H<sub>475-493</sub> due to MCoA binding causes Glu476 and Gln477, which make extensive H-bonds with biotin in MCC<sup>D</sup>, to move away from biotin in MCC<sup>D</sup>. Potential H-bonds are labeled by black dashed lines. **f**, Coordination of biotin at the final active site in MCC-MCoA<sup>D</sup>. Potential H-bonds are labeled by black dashed lines and the numbers near the lines indicate the distances (Å). **g**, Surface representation of the biotin-binding pocket and the MCoA-binding pocket of MCC<sup>D</sup>. The biotin is shown as sticks. **h**,

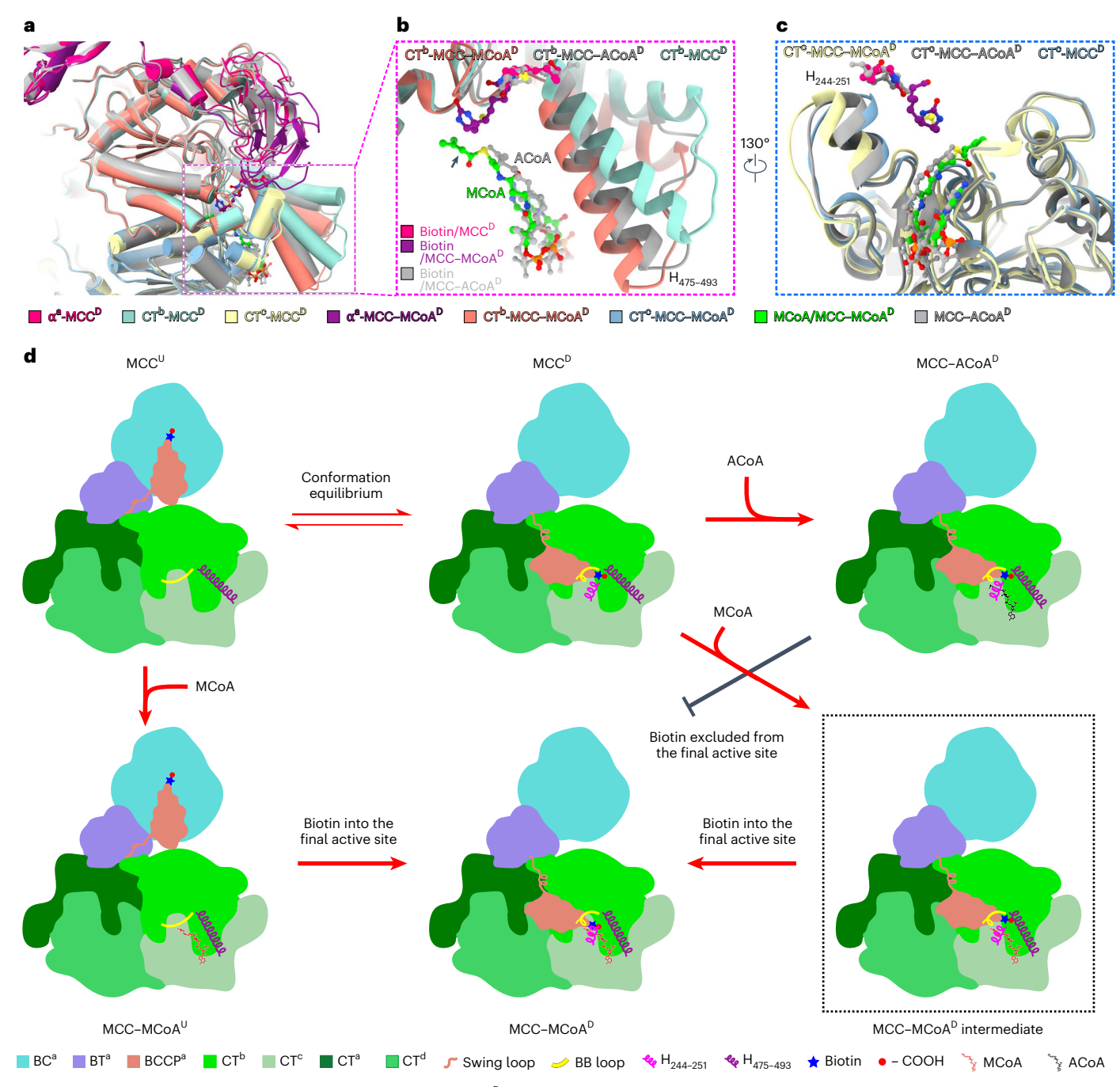
Docking of biotin and MCoA in the MCC–MCoA<sup>D</sup> state into the MCC<sup>D</sup> state. The black triangle indicates the steric hindrance between biotin in the final active site and the CT domain at the MCC<sup>D</sup> state. The MCoA is shown as sticks. **i**, Docking of biotin in the MCC<sup>D</sup> state and MCoA in the MCC–MCoA<sup>D</sup> state into the chimera composed of CT<sup>b</sup>-MCC–MCoA<sup>D</sup> and CT<sup>c</sup>MCC<sup>D</sup>. **j**, Surface representation of the biotin-binding pocket and the MCoA-binding pocket of MCC–MCoA<sup>D</sup>. The subunits of  $\alpha^a$ , CT<sup>b</sup> and CT<sup>c</sup> of MCC<sup>D</sup> are colored in sky blue, limon and light pink, respectively. The subunits of  $\alpha^a$ , CT<sup>D</sup> and CT<sup>c</sup> of MCC<sup>D</sup> are colored in hot pink, light blue and pale yellow, respectively. The subunits of  $\alpha^a$ , CT<sup>D</sup> and CT<sup>c</sup> of MCC–MCoA<sup>D</sup> are colored in pale cyan, light purple and pale green, respectively. The subunits of  $\alpha^a$ , CT<sup>D</sup> and CT<sup>c</sup> of MCC–MCoA<sup>D</sup> are colored in deep purple, salmon and gray blue, respectively. MCoA molecules in MCC–MCoA<sup>D</sup> and MCC–MCoA<sup>D</sup> are colored in deep green and green, respectively.

Notably, the location of biotin in MCC–ACoA<sup>D</sup> is similar to that of biotin in MCC<sup>D</sup>, and the position of  $H_{244\cdot251}$ , the plug to close the biotin-binding pocket, is also closer to that in MCC<sup>D</sup> (Fig. 6b,c). These observations indicate that the shift of  $H_{475\cdot493}$  due to ACoA binding is not sufficient to induce the conformational change of the preactive site and therefore does not allow the release of biotin into the final active site and thus into contact with the substrate. This could explain the poor catalytic activity of MCC toward ACoA<sup>L,18,36</sup>. However, if biotin goes directly into

the final active site without being restricted by the preactive site, MCC may activate nonspecific substrates, that is, CoA esters of organic acids other than MCoA, because of the proximity of the biotin in the final active site to the substrate.

#### **Discussion**

In this work, we applied an optimized method for purifying endogenous biotin-dependent proteins without any gene modification from



 $\begin{tabular}{l} \textbf{Fig. 6} & | \textbf{Schematic of MCC activation. a}, \textbf{Structural comparison of MCC}^D, \textbf{MCC-MCoA}^D \ and \textbf{MCC-ACoA}^D. \textbf{b,c}, \textbf{Close-up view of biotin, MCoA, ACoA and $H_{475-493}$ ($\textbf{b}$) as well as $H_{244-251}$ ($\textbf{c}$) in different states. $\textbf{d}$, Model of the substrate-induced, multi-element synergistic activation of MCC. According to our structures, at least two conformational states of MCC, BCCP in the BC-bound state (MCC^U) and BCCP in the CT-bound state (MCC^D), pre-exist in a substrate-independent dynamic equilibrium in MCC. Multiple structural elements including two loop-to-helix conversions in the swing loop and BB loop, the flipping of BB loop and the presence of $H_{244-251}$ act synergistically to guarantee the specific and smooth binding of biotin on BCCP to the CT domain (MCC^D). However, in the absence of $H_{244-251}$ act synergistically to guarantee the specific and smooth binding of biotin on BCCP to the CT domain (MCC^D). However, in the absence of $H_{244-251}$ act synergistically to guarantee the specific and smooth binding of biotin on BCCP to the CT domain (MCC^D). However, in the absence of $H_{244-251}$ act synergistically to $H_{244-251}$ act synergistically t$ 

the substrate, biotin of MCC at the BCCP in the CT-bound state is trapped in the preactive site that is far away from the substrate (MCC $^{\rm D}$ ). MCoA binding induces the conformational change of  $H_{475.493}$  (MCC–MCoA $^{\rm D}$  intermediate) that reshapes the preactive site to allow biotin into the final active site (MCC–MCoA $^{\rm U}$  and MCC–MCoA $^{\rm D}$ ), while ACoA cannot (MCC–ACoA $^{\rm D}$ ). Therefore, when the correct substrate binds to the enzyme, biotin can be quickly relocated from the preactive site or translocated from the BC-bound state to the final active site to contact the substrate and trigger the subsequent catalytic reaction (MCC–MCoA $^{\rm D}$ ), which ensures the specificity and high efficiency of the enzymatic activity of MCC.

HEK293F cells and obtained eight high-resolution structures of MCC, PCC and PC complexes in different conformational states. We also determined structures of MCC complexes bound to different substrates. These structures provide an integrated picture and important insights into the process of MCC activation (Fig. 6d).

MCC catalysis proceeds through two connected half-reactions catalyzed in distinct and remote active sites<sup>1,58</sup>. The BC domain catalyzes the first half-reaction, where the biotin covalently attached to BCCP is carboxylated<sup>30,33,42</sup>. The CT domain catalyzes the second half-reaction, where the carboxyl group is transferred from the biotin

to the substrate MCoA<sup>31,36</sup>. These two half-reactions are coupled by the intersubunit translocation of the BCCP domain, which traverses a distance greater than 70 Å to transfer the carboxyl group between active sites<sup>36</sup>. One question is that whether BCCP domain positioning exists in a dynamic equilibrium (conformational selection) and/ or is governed by substrate-induced conformational changes<sup>39</sup>. Our structures support the conformational selection model. Based on our structures, MCC has two conformations, BCCP in the BC-bound state (up conformation) and BCCP in the CT-bound state (down conformation), regardless of whether it binds to the substrate or not, that is, the substrate is not required to induce BCCP movement (Fig. 1b and Extended Data Fig. 7). Binding with substrate leads to more down conformations, and up conformations remain (Extended Data Figs. 1 and 7). These phenomena suggest a conformational selection model where multiple conformational states pre-exist in a substrate-independent dynamic equilibrium in MCC and substrate binding serves only to shift the conformation equilibrium to favor biotin binding to CT.

Multiple structural elements act synergistically to guarantee the specific binding and stabilization of biotin on BCCP to the CT domain. With or without MCoA, when BCCP binds to BC, the BB loop at the CT domain covers the biotin-binding pocket to prevent the unfavorable occupancy by any other molecules, thus ensuring that the pocket can only be used by the biotin on the BCCP (Fig. 5a). Along with a conformational change in the swing loop, the BCCP moves away from BC and toward CT (Fig. 3b). The loop-to-helix conversion in the BB loop and the resulted flip of the BB loop opens the biotin-binding pocket and removes its barrier to  $H_{244-251}$  (Fig. 3d). Then the biotin in BCCP can be readily inserted into the pocket and further stabilized by the H-bonds with the BB loop as well as hydrophobic interactions with the BB loop and  $H_{244-251}$  (Fig. 3e–i).

In the absence of the substrate, biotin of MCC at the BCCP in the CT-bound state is trapped in the preactive site that is far away from the substrate (Fig. 5d). Substrate binding is accompanied by a conformational change of H475-493 that reshapes the preactive site to facilitate the final active site conformation for biotin (Fig. 5d-f). The existence of the preactive site could be necessary for the specific recognition of the substrate. Most substrates of biotin-dependent carboxylases are CoA esters of different organic acids, such as ACoA, propionyl-CoA and geranyl-CoA<sup>42</sup>. Comparison of the structures of MCC-MCoA<sup>D</sup> and MCC-ACoA<sup>D</sup> suggests that, although both MCoA and ACoA could bind to MCC, only binding of MCoA can induce biotin from the preactive site to enter the final active site, while ACoA cannot (Fig. 6b,c). This suggests that when there is no substrate, biotin can only stand by at the preactive site, or is in the BC-bound state and cannot contact the substrate; when the correct substrate binds to the enzyme, biotin can be quickly relocated or translocated to the final active site to contact the substrate and trigger the subsequent catalytic reaction, which ensures the specificity and high efficiency of the enzymatic activity of MCC. It should be noted that the alternative hypothesis related to the mechanism of carboxybiotin decarboxylation seems equally plausible. Carboxybiotin will typically decarboxylate in any scenario where the enolate on the ureido oxygen is stabilized and subsequently reprotonated. In many of the accepted mechanisms for carboxyl transfer in the CT domain, carboxybiotin is first decarboxylated and the released CO<sub>2</sub> is subsequently subject to nucleophilic attack from the stabilized enolate of the acceptor substrate. Any scenario where carboxybiotin decarboxylation is promoted in the absence of an acceptor substrate will result in wasteful reaction uncoupling. If BCCP-carboxybiotin positioning is subject to a dynamic equilibrium, as the data in this paper and others suggests, the system is at risk of uncoupling if carboxybiotin can access the CT domain active site and decarboxylate in the absence of an MCC acceptor substrate. A preactive site and a final active site offers a mechanism to protect against enzyme-catalyzing decarboxylation of carboxybiotin in the absence of a bound MCC. In the final active

site conformation, the backbone amide of F407 and A447 are ideally positioned to stabilize the negatively charged ureido oxygen (as is the case in the CT domain of other biotin-dependent carboxylases). No such interactions appear to be poised for stabilization of the ureido oxygen in the preactive site configuration of biotin in the absence of the proper MCC substrate.

#### Online content

Any methods, additional references, Nature Portfolio reporting summaries, source data, extended data, supplementary information, acknowledgements, peer review information; details of author contributions and competing interests; and statements of data and code availability are available at https://doi.org/10.1038/s41594-024-01379-3.

#### References

- Tong, L. Structure and function of biotin-dependent carboxylases. Cell Mol. Life Sci. 70, 863–891 (2013).
- Wei, J. & Tong, L. Crystal structure of the 500-kDa yeast acetyl-CoA carboxylase holoenzyme dimer. Nature 526, 723-727 (2015).
- Chou, C.-Y., Yu, L. P. C. & Tong, L. Crystal structure of biotin carboxylase in complex with substrates and implications for its catalytic mechanism. J. Biol. Chem. 284, 11690–11697 (2009).
- 4. Lombard, J. & Moreira, D. Early evolution of the biotin-dependent carboxylase family. *BMC Evolut. Biol.* **11**, 232 (2011).
- Kim, K.-H. Regulation of mammalian acetyl-coenzyme A carboxylase. Annu. Rev. Nutr. 17, 77–99 (1997).
- McKean, A. L. et al. Molecular characterization of the non-biotin-containing subunit of 3-methylcrotonyl-CoA carboxylase. J. Biol. Chem. 275, 5582–5590 (2000).
- Fu, A. et al. Glucose metabolism and pyruvate carboxylase enhance glutathione synthesis and restrict oxidative stress in pancreatic islets. Cell Rep. 37, 110037 (2021).
- 8. Kumashiro, N. et al. Targeting pyruvate carboxylase reduces gluconeogenesis and adiposity and improves insulin resistance. *Diabetes* **62**, 2183–2194 (2013).
- Lao-On, U., Attwood, P. V. & Jitrapakdee, S. Roles of pyruvate carboxylase in human diseases: from diabetes to cancers and infection. J. Mol. Med. 96, 237–247 (2018).
- Yang, J., Chi, Y., Burkhardt, B. R., Guan, Y. & Wolf, B. A. Leucine metabolism in regulation of insulin secretion from pancreatic beta cells. *Nutr. Rev.* 68, 270–279 (2010).
- Anderson, M. D., Che, P., Song, J., Nikolau, B. J. & Wurtele, E. S. 3-Methylcrotonyl-coenzyme A carboxylase is a component of the mitochondrial leucine catabolic pathway in plants. *Plant Physiol.* 118, 1127–1138 (1998).
- Baumgartner, M. R. et al. The molecular basis of human 3-methylcrotonyl-CoA carboxylase deficiency. J. Clin. Invest. 107, 495–504 (2001).
- Gallardo, M. E. et al. The molecular basis of 3-methylcrotonylglycinuria, a disorder of leucine catabolism. Am. J. Hum. Genet 68, 334–346 (2001).
- Stadler, S. C. et al. Newborn screening for 3-methylcrotonyl-CoA carboxylase deficiency: population heterogeneity of MCCA and MCCB mutations and impact on risk assessment. *Hum. Mutat.* 27, 748–759 (2006).
- Chu, C. H. & Cheng, D. Expression, purification, characterization of human 3-methylcrotonyl-CoA carboxylase (MCCC). *Protein Expr. Purif.* 53, 421–427 (2007).
- Huang, C. S. et al. Crystal structure of the alpha (6) beta (6) holoenzyme of propionyl-coenzyme A carboxylase. Nature 466, 1001–1005 (2010).
- 17. Desviat, L. R. et al. Propionic acidemia: mutation update and functional and structural effects of the variant alleles. *Mol. Genet Metab.* **83**, 28–37 (2004).

- Wongkittichote, P., Ah Mew, N. & Chapman, K. A. Propionyl-CoA carboxylase—a review. Mol. Genet Metab. 122, 145–152 (2017).
- Grünert, S. C. et al. 3-methylcrotonyl-CoA carboxylase deficiency, clinical, biochemical, enzymatic and molecular, studies in 88 individuals. Orphanet J. Rare Dis. https://doi.org/10.1186/1750-1172-7-31 (2012).
- Hoschle, B., Gnau, V. & Jendrossek, D. Methylcrotonyl-CoA and geranyl-CoA carboxylases are involved in leucine/isovalerate utilization (Liu) and acyclic terpene utilization (Atu), and are encoded by liuB/liuD and atuC/atuF, in Pseudomonas aeruginosa. Microbiol. 151, 3649–3656 (2005).
- Haase, F. C., Beegen, H. & George Allen, S. H. Propionyl-coenzyme A carboxylase of Mycobacterium smegmatis. Eur. J. Biochem. 140, 147–151 (1984).
- Rivera-Barahona, A. et al. Identification of 34 novel mutations in propionic acidemia: functional characterization of missense variants and phenotype associations. *Mol. Genet. Metab.* 125, 266–275 (2018).
- Armstrong, A. J. et al. A novel small molecule approach for the treatment of propionic and methylmalonic acidemias. *Mol. Genet. Metab.* 133, 71–82 (2021).
- Marin-Valencia, I., Roe, C. R. & Pascual, J. M. Pyruvate carboxylase deficiency: mechanisms, mimics and anaplerosis. *Mol. Genet. Metab.* 101, 9–17 (2010).
- Wallace, J. C., Jitrapakdee, S. & Chapman-Smith, A. Pyruvate carboxylase. Int. J. Biochem. Cell Biol. 30, 1–5 (1998).
- Xiang, S. & Tong, L. Crystal structures of human and Staphylococcus aureus pyruvate carboxylase and molecular insights into the carboxyltransfer reaction. Nat. Struct. Mol. Biol. 15, 295–302 (2008).
- Cappel, D. A. et al. Pyruvate-carboxylase-mediated anaplerosis promotes antioxidant capacity by sustaining TCA cycle and redox metabolism in liver. Cell Metab. 29, 1291–1305 e1298 (2019).
- Choi, P. H. et al. Structural and functional studies of pyruvate carboxylase regulation by cyclic di-AMP in lactic acid bacteria. Proc. Natl Acad. Sci. USA 114, E7226–E7235 (2017).
- Sellers, K. et al. Pyruvate carboxylase is critical for non-small-cell lung cancer proliferation. J. Clin. Invest. 125, 687–698 (2015).
- Broussard, T. C., Pakhomova, S., Neau, D. B., Bonnot, R. & Waldrop, G. L. Structural analysis of substrate, reaction intermediate, and product binding in *Haemophilus influenzae* biotin carboxylase. *Biochemistry* 54, 3860–3870 (2015).
- 31. Healy, S. et al. Structural impact of human and *Escherichia* coli biotin carboxyl carrier proteins on biotin attachment. *Biochemistry* **49**, 4687–4694 (2010).
- Reddy, M. C. et al. Structure, activity, and inhibition of the carboxyltransferase beta-subunit of acetyl coenzyme A carboxylase (AccD6) from Mycobacterium tuberculosis. Antimicrob. Agents Chemother. 58, 6122–6132 (2014).
- Novak, B. R., Moldovan, D., Waldrop, G. L. & de Queiroz, M. S. Behavior of the ATP grasp domain of biotin carboxylase monomers and dimers studied using molecular dynamics simulations. *Proteins* 79, 622–632 (2011).
- Martin St, M. et al. Domain architecture of pyruvate carboxylase, a biotin-dependent multifunctional enzyme. Science 317, 1076–1079 (2007).
- 35. Fawaz, M. V., Topper, M. E. & Firestine, S. M. The ATP-grasp enzymes. *Bioorg. Chem.* **39**, 185–191 (2011).
- Huang, C. S., Ge, P., Zhou, Z. H. & Tong, L. An unanticipated architecture of the 750-kDa alpha6beta6 holoenzyme of 3-methylcrotonyl-CoA carboxylase. *Nature* 481, 219–223 (2011).
- Lietzan, A. D. et al. Interaction between the biotin carboxyl carrier domain and the biotin carboxylase domain in pyruvate carboxylase from *Rhizobium etli*. *Biochemistry* 50, 9708–9723 (2011).

- Lopez-Alonso, J. P. et al. CryoEM structural exploration of catalytically active enzyme pyruvate carboxylase. *Nat. Commun.* 13, 6185 (2022).
- 39. Hakala, J. H., Laseke, A. J., Koza, A. L. & St Maurice, M. Conformational selection governs carrier domain positioning in *Staphylococcus aureus* pyruvate carboxylase. *Biochemistry* **61**, 1824–1835 (2022).
- Liu, Y., Budelier, M. M., Stine, K. & St Maurice, M. Allosteric regulation alters carrier domain translocation in pyruvate carboxylase. *Nat. Commun.* 9, 1384 (2018).
- 41. Mochalkin, I. et al. Structural evidence for substrate-induced synergism and half-sites reactivity in biotin carboxylase. *Protein Sci.* **17**, 1706–1718 (2008).
- 42. Waldrop, G. L., Holden, H. M. & St Maurice, M. The enzymes of biotin dependent CO(<sub>2</sub>) metabolism: what structures reveal about their reaction mechanisms. *Protein Sci.* **21**, 1597–1619 (2012).
- Chou, C. Y. & Tong, L. Structural and biochemical studies on the regulation of biotin carboxylase by substrate inhibition and dimerization. J. Biol. Chem. 286, 24417–24425 (2011).
- Lee, J. K. J. et al. CryoEM reveals oligomeric isomers of a multienzyme complex and assembly mechanics. J. Struct. Biol. https://doi.org/10.1016/j.yjsbx.2023.100088 (2023).
- Diacovich, L. et al. Crystal structure of the beta-subunit of acyl-CoA carboxylase structure-based engineering of substrate specificity. *Biochemistry* 43, 14027–14036 (2004). 10.1021.
- 46. Scheffen, M. et al. A new-to-nature carboxylation module to improve natural and synthetic  $CO_2$  fixation. *Nat. Catal.* **4**, 105–115 (2021).
- Chai, P. et al. Mechanistic insight into allosteric activation of human pyruvate carboxylase by acetyl-CoA. *Mol. Cell* 82, 4116–4130 e4116 (2022).
- 48. Lietzan, A. D. & St Maurice, M. A substrate-induced biotin binding pocket in the carboxyltransferase domain of pyruvate carboxylase. *J. Biol. Chem.* **288**, 19915–19925 (2013).
- Lietzan, A. D., Lin, Y. & St Maurice, M. The role of biotin and oxamate in the carboxyltransferase reaction of pyruvate carboxylase. Arch. Biochem Biophys. 562, 70–79 (2014).
- Lietzan, A. D. & St Maurice, M. Insights into the carboxyltransferase reaction of pyruvate carboxylase from the structures of bound product and intermediate analogs. *Biochem. Biophys. Res. Commun.* 441, 377–382 (2013).
- Yu, L. P. et al. A symmetrical tetramer for S. aureus pyruvate carboxylase in complex with coenzyme A. Structure 17, 823–832 (2009).
- Sureka, K. et al. The cyclic dinucleotide c-di-AMP is an allosteric regulator of metabolic enzyme function. Cell 158, 1389–1401 (2014).
- Rybak, J. N., Scheurer, S. B., Neri, D. & Elia, G. Purification of biotinylated proteins on streptavidin resin: a protocol for quantitative elution. *Proteomics* 4, 2296–2299 (2004).
- Barden, R. E. et al. Structural properties of pyruvate carboxylases from chicken liver and other sources. Proc. Natl Acad. Sci. USA 72, 4308–4312 (1975).
- 55. Swack, J. A., Zander, G. L. & Utter, M. F. Use of avidin-sepharose to isolate and idenify biotin polypeptides from crude extracts. *Anal. Biochem* **87**, 114–126 (1978).
- 56. Libor, S., Warwick, R. & Sundaram, T. K. Binding behaviour of pyruvate carboxylase from *Bacillus stearothermophilus* on sepharose–avidin. *FEBS Lett.* **57**, 34–36 (1975).
- Salie, M. J. & Thelen, J. J. Regulation and structure of the heteromeric acetyl-CoA carboxylase. *Biochim Biophys. Acta* 1861, 1207–1213 (2016).
- Tong, L. Striking diversity in holoenzyme architecture and extensive conformational variability in biotin-dependent carboxylases. Adv. Protein Chem. Struct. Biol. 109, 161–194 (2017).

**Publisher's note** Springer Nature remains neutral with regard to jurisdictional claims in published maps and institutional affiliations.

Springer Nature or its licensor (e.g. a society or other partner) holds exclusive rights to this article under a publishing agreement with the author(s) or other rightsholder(s); author self-archiving

of the accepted manuscript version of this article is solely governed by the terms of such publishing agreement and applicable law.

@ The Author(s), under exclusive licence to Springer Nature America, Inc. 2024

#### Methods

#### Cell culture

HEK293F (Thermo Fisher Scientific, cat. no. 11625019) cells were cultured and collected in the same way as our previous research<sup>59</sup>.

#### Mitochondria isolation

Mitochondria were isolated in the same way as our previous research<sup>59</sup>.

#### MCC, PC and PCC complex purification

Buffer B contained 20 mM MOPS pH 7.4, 150 mM KCI, 10% (v/v) glycerol and 1 mM phenylmethylsulfonyl fluoride. For the purification of MCC and PC, mitochondria were suspended with buffer B with the addition of 1% (v/v) digitonin (BIOSYNTH, cat. no. D3200) and incubated for 2 h. Then the lysate was centrifuged at 150.000g for 30 min at 4 °C. Strep-Tactin affinity resins (IBA Lifesciences) with a bed volume of 2 ml were added into the supernatant and incubated for 1 h at 4 °C in a 50 ml tube. The resins were washed with 300 ml washing buffer (20 mM MOPS pH 7.4, 150 mM KCI, 10% (v/v) glycerol). The complex was eluted by washing buffer containing 50 mM biotin (Sigma-Aldrich) and concentrated to 100 µl using a 100 kDa cut-off centrifugal filter (Millipore). The MCC and PC complexes were subsequently purified via gel filtration using a Superose 6 Increase 3.2/300 GL column (GE Healthcare). Fractions were collected for SDS-PAGE analysis, and those containing MCC and PC were further used for cryo-EM sample preparation and substrate binding.

The purification of PCC was almost the same as that of MCC and PC, except that the incubation time for mitochondria with digitonin was extended from 2 to 4 h. We found that 2 h of incubation was sufficient to extract MCC and PC, but not PCC, as shown in Extended Data Fig. 1a. We could obtain PCC when the incubation time was extended to 4 h. Therefore, we could observe three proteins together in Extended Data Fig. 2a. We speculated that PCC might interact with certain membrane-associated proteins and thus required prolonged detergent treatment to obtain it.

#### Chemical crosslinking

The crosslinked MCC complex and PC complex were obtained by adding 0.1% glutaraldehyde (Sigma-Aldrich, cat. no. 359127) for incubation for 1 h at room temperature. The crosslinking reaction was quenched by the addition of 50 mM Tris-HCl (pH 8.0). Then the crosslinked complexes were purified by gel filtration using a Superose 6 Increase 3.2/300 GL column (GE Healthcare).

#### Substrate binding

For this, 0.5 mM MCoA (Sigma-Aldrich) or ACoA (Sigma-Aldrich) was added to the purified MCC complex in the reaction buffer (20 mM MOPS pH 7.4,150 mM KCl). After incubation on ice for 1 h, the mixture was directly used for cryo-EM sample preparation.

#### Cryo-EM sample preparation and data collection

The sample (4  $\mu$ l) was applied to glow-discharged grids (R 1.2/1.3 Au, 300 mesh, Quantifoil). Grids were bolted by the FEI Mark IV Vitrobot for 3.5 s and plunged into liquid ethane. The datasets of the MCC and PC complexes with crosslinking and the PCC complex were collected on a Titan Krios G3i transmission electron microscope (TEM) (Thermo Fisher Scientific) operated at 300 kV with a Gatan K3 Summit direct electron detector and GIF Quantum imaging energy filter. The dataset of the MCC complex with MCoA was collected on a Titan Krios TEM (Thermo Fisher Scientific) operated at 300 kV with a Gatan K2 Summit direct electron detector. The dataset of the MCC complex with ACoA was collected on a Talos Arctica TEM (Thermo Fisher Scientific) operated at 200 kV with a Gatan K2 Summit direct electron detector. All images were acquired with AutoEMation (written by J. Lei) 60. Two datasets from the MCC complex and the PC complex with crosslinking and the PCC complex were collected at a nominal magnification

of ×81,000. The pixel size was 1.09 Å/pixel with defocus between -1.3 and  $-1.8~\mu m$ . The dataset of the MCC complex with MCoA was collected at a nominal magnification of ×29,000. The pixel size was 0.97 Å/pixel with defocus between -1.3 and  $-1.8~\mu m$ . The total dose rate on the detector was about 50 e $^-$ /Å $^2$  with a total exposure time of 2.13 s. The dataset of the MCC complex with ACoA was collected at a nominal magnification of ×45,000. The pixel size was 0.94 Å/pixel with defocus between -1.3 and  $-1.8~\mu m$ . The total dose rate on the detector was about 50 e $^-$ /Å $^2$  with a total exposure time of 4.32 s. Each micrograph stack contained 32 frames. Each micrograph was corrected for subregion motion correction and dose weighted using UCSF MotionCor2 (ref. 61).

#### Single-particle image processing

The dataset containing MCC and PC included 1,245 micrographs. CryoSPARC<sup>62</sup> was used for data processing. First, the contrast transfer function (CTF) parameters of all micrographs were estimated by Patch CTF estimation (Mulit). Then 100 particles were manually picked and applied to two-dimensional (2D) classification. All 2D classes can separate two kinds, PC and MCC. For PC, good 2D classes were selected and used as the template for template picker. Then 60,113 particles were picked with a particle diameter of 280 Å. After 2D classification, 49,360 particles were selected to do ab initio reconstruction. Three different classes were obtained and two good classes accounted for 45.1 and 46% of total particles. The particles of two good classes were re-extracted with bin1, and applied to 2D classification again. Next, 21,326 and 21,450 particles were selected and generated two reconstructions at 3.83 and 5.63 Å resolutions after refinement with D2 symmetry for  $PC^{D/noBC}$ and PCD/intact, respectively. For MCC, after 2D classification, 422,660 particles were selected to perform ab initio reconstruction. Three  $different\, classes\, were\, obtained\, and\, the\, best\, class\, accounted\, for\, 65.0\%$ of total particles. These particles were applied to refinement with C1 symmetry. Then 3D classification was performed. Five different classes were obtained from 3D classification. Three different states can be distinguished from 3D classification. For state one, all particles were re-extracted with bin1. Next, 53,474 particles were obtained and applied to do refinement with D3 symmetry. The resolution of MCC<sup>D</sup> was 2.51 Å based on the Fourier shell correlation (FSC) 0.143 criteria. For state two, all particles were re-extracted with bin1. Then 63,281 particles were obtained and applied to do refinement with D3 symmetry. The resolution of MCC<sup>U</sup> was 2.52 Å based on the FSC 0.143 criteria. Two other classes were selected to perform 3D classification again. Four different classes were obtained. The 15.5% part was re-extracted with bin1, and 10,701 particles were obtained and applied to refinement with C2 symmetry, which produced the reconstruction of MCC<sup>H2</sup> at 3.88 Å resolution. The 2.0% part was re-extracted with bin1, and 1,474 particles were obtained and applied to refinement with D3 symmetry, which produced the reconstruction of MCC<sup>Core-Dimer</sup> at 4.16 Å resolution. The 77.9% part was re-extracted with bin1, and 53,820 particles were obtained and applied to refinement with C2 symmetry, which produced the reconstruction of MCCH1 at 2.70 Å resolution. All resolutions were based on the FSC 0.143 criteria.

For the PCC complex dataset, 4,198 micrographs were imported into cryoSPARC  $^{62}$ . Patch CTF estimations (Mulit) were performed on all micrographs. Then 300 particles were manually picked and applied to 2D classification. Good classes were selected and served as templates to run the template picker. In this step, 1,011,596 particles were picked with the particle diameter of 360 Å. After 2D classification, 516,854 good particles were selected to perform ab initio reconstruction with C1 symmetry, which produced four different classes. The particles of the best class, representing 16.5% of total particles, were re-extracted with bin1 and applied to refinement with D3 symmetry. The resolution of PCC  $^{\rm D}$  was 2.59 Å.

The dataset of MCoA-bound MCC had 2,048 micrographs. Micrographs were imported into cryoSPARC<sup>62</sup>. Patch CTF estimations (Mulit)

were performed on all micrographs. Particles were picked through a template picker. The template came from the data processing of the MCC and PC datasets. In total, 843,319 particles were picked. After 2D classification, 827,545 particles selected to perform ab initio reconstruction with C1 symmetry, which generated two different classes. The good class accounted for 90.2% of total particles. These particles were re-extracted with bin1, and applied to refinement with C1 symmetry. 3D classification was performed to the result of refinement and produced three different classes. The 36.6% part was good for the next step. The 29.1 and 34.4% parts were merged and applied to 3D classification again. The good class accounting for 32.2% was merged with the 36.6% part from the last step and applied to refinement with C1 symmetry. Four different classes were obtained and could be separated into three states illustrated with a red mark, green mark and purple mark in Extended Data Fig. 7c. Refinement with D3 symmetry was carried out on the purple state, and resulted in the reconstruction of MCoAD at 2.81 Å resolution. The remaining particles were further applied to several rounds of 3D classifications as detailed in Extended Data Fig. 7c. Finally, we obtained three reconstructions of MCoA<sup>U</sup>, MCoA<sup>HI</sup> and MCoA<sup>H2</sup> at 2.98, 3.20 and 3.49 Å, respectively.

Next, 854 micrographs of ACoA-bound MCC were collected and imported into cryoSPARC for Patch CTF estimation (Mulit). Particles were picked through template picker. The template came from the data processing of the MCC and PC datasets. In total, 203,299 particles were picked. After 2D classification, good particles were selected to do ab initio reconstruction with C1 symmetry. Two different classes were obtained. The best class obtained 31,050 particles and accounted for 90.2% of total particles. The particles were applied to refinement with C1 symmetry. 3D classification was performed to the result of refinement. Six different classes were obtained. The 15.6, 16.1 and 16.5% parts were merged and re-applied to refinement. 3D classification was performed again. The 75.8% part of the total particles was good. Refinement of these particles with C1 symmetry followed with D3 symmetry generated the reconstruction of ACoAD at 3.52 Å resolution.

#### Model building and refinement

The homology model of hMCC-α and hMCC-β subunits were downloaded from the AlphaFold database. These models were first rigid-body fitted into the maps of MCCD, MCCU, MCCH1, MCCH2, MCC-MCoA<sup>H1</sup>, MCC-MCoA<sup>H2</sup>, MCC-MCoA<sup>U</sup>, MCC-MCoA<sup>D</sup> and MCC-ACoA<sup>D</sup> using UCSF Chimera<sup>63</sup>. To adjust the positions of the BC and BCCP domains, they were segmented out from the homology models and rigid-body fitted again into the maps of MCC<sup>U</sup>, MCC<sup>D</sup>, MCC<sup>H1</sup>, MCC<sup>H2</sup>, MCC-MCoA<sup>H1</sup>, MCC-MCoA<sup>H2</sup>, MCC-MCoA<sup>U</sup>, MCC-MCoA<sup>D</sup> and MCC-ACoAD. Then the gaps between the BC and BT/BCCP domains were fixed according to the density in COOT<sup>64</sup>. The backbone and side chains of the model underwent manual adjustment and refinement in COOT. A very clear biotin density was identified in MCC<sup>D</sup> and MCC-MCoA<sup>D</sup>. Meanwhile, a very clear MCoA density was identified in the MCC-MCoAH1, MCC-MCoA<sup>H2</sup>, MCC-MCoA<sup>U</sup> and MCC-MCoA<sup>U</sup> β subunits and a very clear ACoA density was identified in MCC-ACoA<sup>D</sup>. The MCC- $\alpha$ /MCC- $\beta$ dimer model of human MCC with ligand was subjected to real space refinement in PHENIX<sup>65</sup>. Finally, the whole human MCC α6β6 models were obtained from symmetry expansion by docking the refined MCC- $\alpha$ /MCC- $\beta$  dimer model into the density maps using UCSF Chimera. The geometries of final models were validated with comprehensive model validation section in PHENIX and detailed information is listed in Tables 1 and 2.

The homology model of hPC was downloaded from the AlphaFold database. The model was first rigid-body fitted into the PC  $^{D/noBC}$  map and PC  $^{D/intact}$  using UCSF Chimera, showing good agreement with the density data in both, except for the missing BC domain in PC  $^{D/noBC}$ . The backbone and side chains of the model also underwent manual adjustment and refinement in COOT. The PC tetramer model with ligand was subjected to real space refinement in PHENIX. The geometries of final

models were validated with comprehensive model validation section in PHENIX and detailed information is listed in Table 1.

The homology models of hPCC-α and hPCC-β subunits were downloaded from the AlphaFold database. They were first rigid-body fitted into the unsharpened map using UCSF Chimera, showing good agreement with the density data, except for the BC-B subdomain of BC domain and BCCP domain. Then, the BC-B subdomain and BCCP domain models were segmented out from the homology model and rigid-body fitted again into the unsharpened map using UCSF Chimera. Then the gaps between the BC/BC-B and BT/BCCP domains were fixed according to the density data in COOT<sup>64</sup>. The backbone and side chains of the model underwent manual adjustment and refinement in COOT. A very clear biotin density was identified in the PCC-β subunit. The PCC-α/PCC-β dimer model of human PCC with ligand was subjected to real space refinement in PHENIX<sup>65</sup>. Finally, the whole human PCC<sup>D</sup> α6β6 model was obtained from symmetry expansion by docking the refined PCC- $\alpha$ /PCC- $\beta$  dimer model into the density map using UCSF Chimera. The geometries of the final model were validated with comprehensive model validation section in PHENIX and detailed information is listed in Table 1. All figures were prepared with Pymol<sup>66</sup> and Chimera.

#### **Recombinant MCC complex purification**

The DNA of MCC $\beta$ -Flag and MCC $\alpha$  were synthesized by General Biosystems Co. Ltd (China) and cloned into pCMV-3 vector. The plasmids of MCC $\beta$ -L241R-Flag and MCC $\beta$ -A242F-Flag were conducted by the PerfectStart Green PCR SuperMix (Trans). The primer sequences are listed as follows:

MCCβ-L241R-F: GCAAGCAGGGTACCATTTTCTTCGCAGGA MCCβ-L241R-R: GTCCTGCGAAGAAAATGGTACCCTGCTTG MCCβ-A242F-F: AAGCAGGGTACCATTTTCTTGTTCGGACC MCCβ-A242F-R: GTCCGAACAAGAAAATGGTACCCTGCTTG

Here, HEK293F (Invitrogen) cells were cultured as described in the previous paper  $^{59}$ . When cell density reached 2 × 106 cells per ml, the plasmids of of MCC $\beta$ -Flag and MCC $\alpha$ , MCC $\beta$ -L241R-Flag and MCC $\alpha$ , MCC $\beta$ -A242F-Flag and MCC $\alpha$  were transfected into cells independently. After cultivation for 48 h, cells were collected and washed once with PBS (137 mM NaCl, 2.7 mM KCl, 4.3 mM Na $_2$ HPO $_4$ , 1.4 mM KH $_2$ PO $_4$ , pH 7.2). Cell pellets were frozen in liquid nitrogen and stored at  $-80\,^{\circ}\text{C}$ .

Mitochondria isolation was performed as previously described  $^{59}$ . Mitochondria were lysed by 1% (v/v) digitonin (BIOSYNTH, cat. no. D3200) for 2 h. Then the mixture was centrifuged at 150,000g for 30 min at 4 °C. Flag beads (Sigma) were added into the supernatant and incubated for 1 h at 4 °C. The beads were washed with 300 ml of washing buffer (20 mM MOPS pH 7.4,150 mM KCl,10% (v/v) glycerol). The complex was eluted with 5  $\mu g$  ml $^{-1}$  Flag peptide (Genscript) and concentrated to 100  $\mu$ l using a 100 kDa cut-off centrifugal filter (Millipore). The complex was then purified by gel filtration with a Superose 6 Increase 3.2/300 GL column (GE Healthcare). The purified proteins were collected for the enzyme activity assays.

#### **Enzyme activity assays**

MCC enzyme activity assays were performed according to the method by Cheng  $^{15}$  and Lau  $^{67}$  with modifications. The assay buffer was composed of 50 mM MOPS pH 7.4, 5 mM MgCl  $_2$ , 150 mM KCl, 0.02 mM MCoA and 5 mM NaHCO  $_3$ . The reactions were carried out in a final volume of 100  $\mu$ l containing 0.4  $\mu$ M protein. Then, 1 mM ATP was added to initiate the reaction and further incubated for 30 min at 25 °C. The reaction was quenched by 400  $\mu$ l CH  $_3$ OH. The quenched reaction was centrifuged to remove the precipitate, and the supernatant was applied to a solid-phase extraction column (Oasis HLB)  $^{68}$ , which was then washed with 1 ml of H  $_2$ O to remove the salt. Finally, MCoA was eluted with 0.5 ml of elution solution (25 mM CH  $_3$ COONH  $_4$  in CH  $_3$ OH) and dried under nitrogen. The precipitate was resuspended in 5% (w/v) 5-sulfosalicylic acid dihydrate and was then ready for liquid chromatography with mass spectrometry (LC–MS) analysis.

#### LC-MS analysis

The ultra-high-performance LC system was furnished with a heated electrosprayionization probe and coupled to a Q-Exactive HFX orbitrap mass spectrometer (Thermo Fisher). MCoA samples were separated by a BEH C18 100 × 2.1 mm 1.7 um column (Waters). Then 100% H<sub>2</sub>O (5 mM NH<sub>4</sub>HCO<sub>3</sub>) and 100% CAN composed two mobile phases in a binary solvent system. The flow rate was 300 μl min<sup>-1</sup> and lasted for 12 min. The temperatures were 30 and 10 °C for the column chamber and sample tray, respectively. In positive ion mode with data dependent tandem MS acquisition, the data with mass ranges of m/z 300–1,500 were collected. The full scan and fragment spectra were collected with resolutions of 60,000 and 15,000, respectively. The source parameters used were as follows: spray voltage 3,200 V, capillary temperature 320 °C, heater temperature 300 °C, sheath gas flow rate 35 a.u. and auxiliary gas flow rate 10 a.u. Data were analyzed by the software Xcalibur (Thermo Fisher). A mass tolerance of 5 ppm was applied for the precursor search. The automatic area of the peak of MCoA was regarded as the amount of MCoA.

#### **Reporting summary**

Further information on research design is available in the Nature Portfolio Reporting Summary linked to this article.

#### **Data availability**

Atomic coordinates and EM density maps of MCC<sup>U</sup> (Protein Data Bank (PDB) 8JAK, EMD-36128), MCC<sup>D</sup> (PDB 8JAW, EMD-36136), MCC<sup>H1</sup> (PDB 8J7D, EMD-36038), MCC<sup>H2</sup> (PDB 8J78, EMD-36034), MCC<sup>Core-Dimer</sup> (PDB 8J73, EMD-36024), PC<sup>D/noBC</sup> (PDB 8J70, EMD-36044), PC<sup>D/intact</sup> (PDB 8HWL, EMD-35059), PCC<sup>D</sup> (PDB 7YBU, EMD-33729), MCC-MCoA<sup>U</sup> (PDB 8JXL, EMD-36704), MCC-MCoA<sup>D</sup> (PDB: 8J4Z, EMD-35980), MCC-MCoA<sup>H1</sup> (PDB 8JXN, EMD-36706), MCC-MCoA<sup>H2</sup> (PDB 8JXM, EMD-36705) and MCC-ACoA<sup>D</sup> (PDB 8K2V, EMD-36840) have been deposited in the PDB (www.rcsb.org) and the Electron Microscopy Data Bank (www.ebi.ac.uk/pdbe/emdb/).

#### References

- Su, J. et al. Structural basis of Tom20 and Tom22 cytosolic domains as the human TOM complex receptors. *Proc. Natl Acad.* Sci. USA 119, e2200158119 (2022).
- Lei, J. & Frank, J. Automated acquisition of cryo-electron micrographs for single particle reconstruction on an FEI Tecnai electron microscope. J. Struct. Biol. 150, 69–80 (2005).
- Zheng, S. Q. et al. MotionCor2: anisotropic correction of beam-induced motion for improved cryo-electron microscopy. *Nat. Methods* 14, 331–332 (2017).
- 62. Punjani, A., Rubinstein, J. L., Fleet, D. J. & Brubaker, M. A. cryoSPARC: algorithms for rapid unsupervised cryo-EM structure determination. *Nat. Methods* **14**, 290–296 (2017).
- Pettersen, E. F. et al. UCSF Chimera—a visualization system for exploratory research and analysis. J. Comput. Chem. 25, 1605–1612 (2004).

- 64. Emsley, P., Lohkamp, B., Scott, W. G. & Cowtan, K. Features and development of Coot. *Acta Crystallogr. D. Biol. Crystallogr.* **66**, 486–501 (2010).
- 65. Adams, P. D. et al. PHENIX: a comprehensive Python-based system for macromolecular structure solution. *Acta Crystallogr. D. Biol. Crystallogr.* **66**, 213–221 (2010).
- 66. Delano, W. The PyMOL Molecular Graphics System (DeLano Scientific, 2002).
- 67. Lau, E. P., Cochran, B. C. & Fall, R. R. Isolation of 3-methylcrotonylcoenzyme A carboxylase from bovine kidney. *Arch. Biochem. Biophys.* **205**, 352–359 (1980).
- 68. Basu, S. S. & Blair, I. A. SILEC: a protocol for generating and using isotopically labeled coenzyme A mass spectrometry standards. *Nat. Protoc.* **7**, 1–11 (2011).

#### Acknowledgements

We thank the staff at the Tsinghua University Branch of the National Protein Science Facility (Beijing) for technical support on the cryo-EM and high-performance computation platforms. This work was supported by the National Natural Science Foundation of China (grant nos. 32071192 to S.-F.S., 92254306 to S.S. and 31825009 to H.-W.W.).

#### **Author contributions**

S.-F.S., H.-W.W. and S.S. supervised the project. J.S. and S.S. designed the experiments. J.S., X.T. and Z.W. purified the proteins and prepared the cryo-EM samples. J.S. and H.C. collected the cryo-EM data. D.L. and X.T. built the atomic models. J.S., X.T., D.L., S.S. and S.-F.S. analyzed the structures. J.S., X.T. and D.L. wrote the initial draft. S.S and S.-F.S. edited the manuscript.

#### **Competing interests**

The authors declare no competing interests.

#### **Additional information**

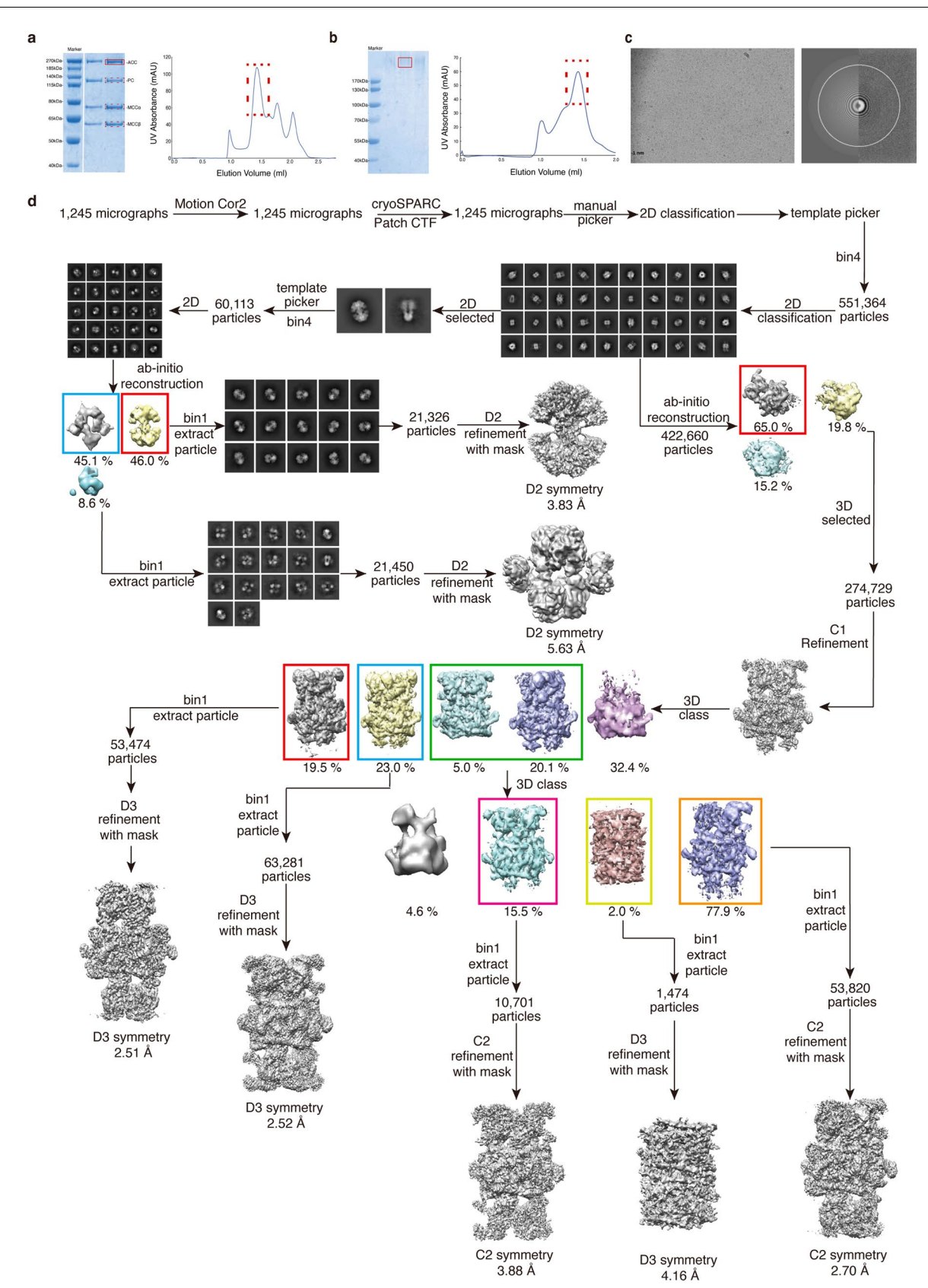
**Extended data** is available for this paper at https://doi.org/10.1038/s41594-024-01379-3.

**Supplementary information** The online version contains supplementary material available at https://doi.org/10.1038/s41594-024-01379-3.

**Correspondence and requests for materials** should be addressed to Shan Sun, Hong-Wei Wang or Sen-Fang Sui.

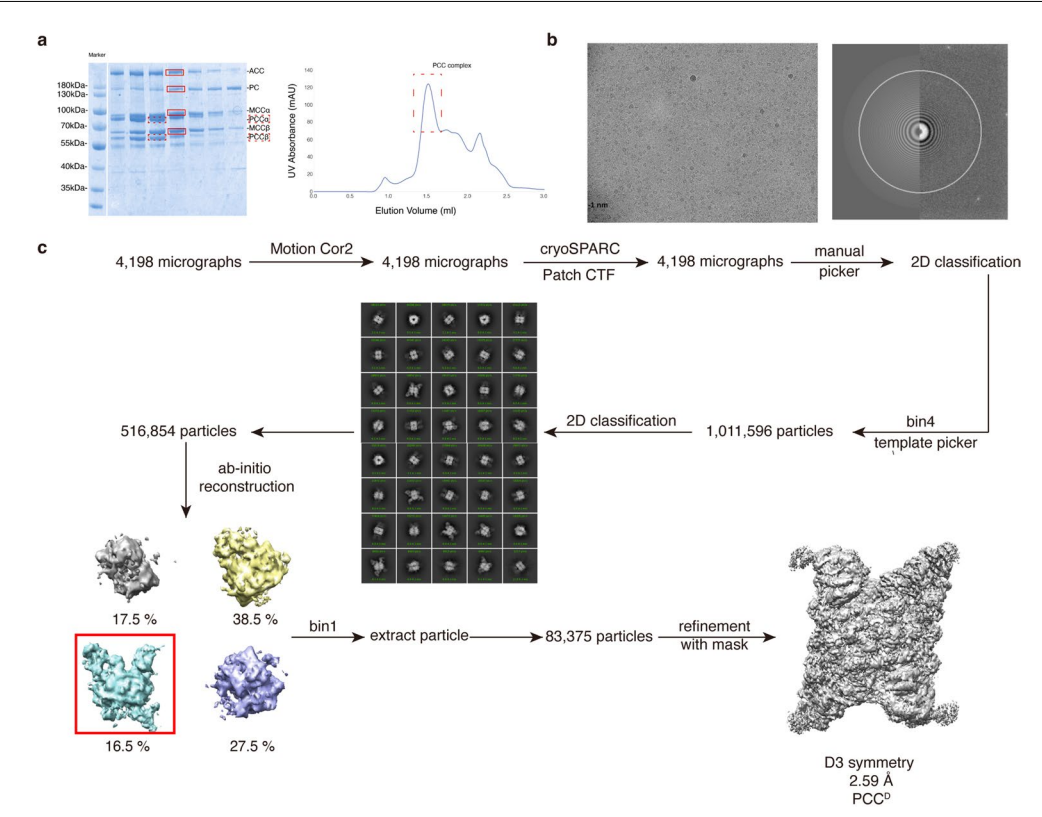
Peer review information Nature Structural & Molecular Biology thanks Martin St. Maurice and the other, anonymous, reviewer(s) for their contribution to the peer review of this work. Primary Handling Editor: Dimitris Typas, in collaboration with the Nature Structural & Molecular Biology team.

**Reprints and permissions information** is available at www.nature.com/reprints.



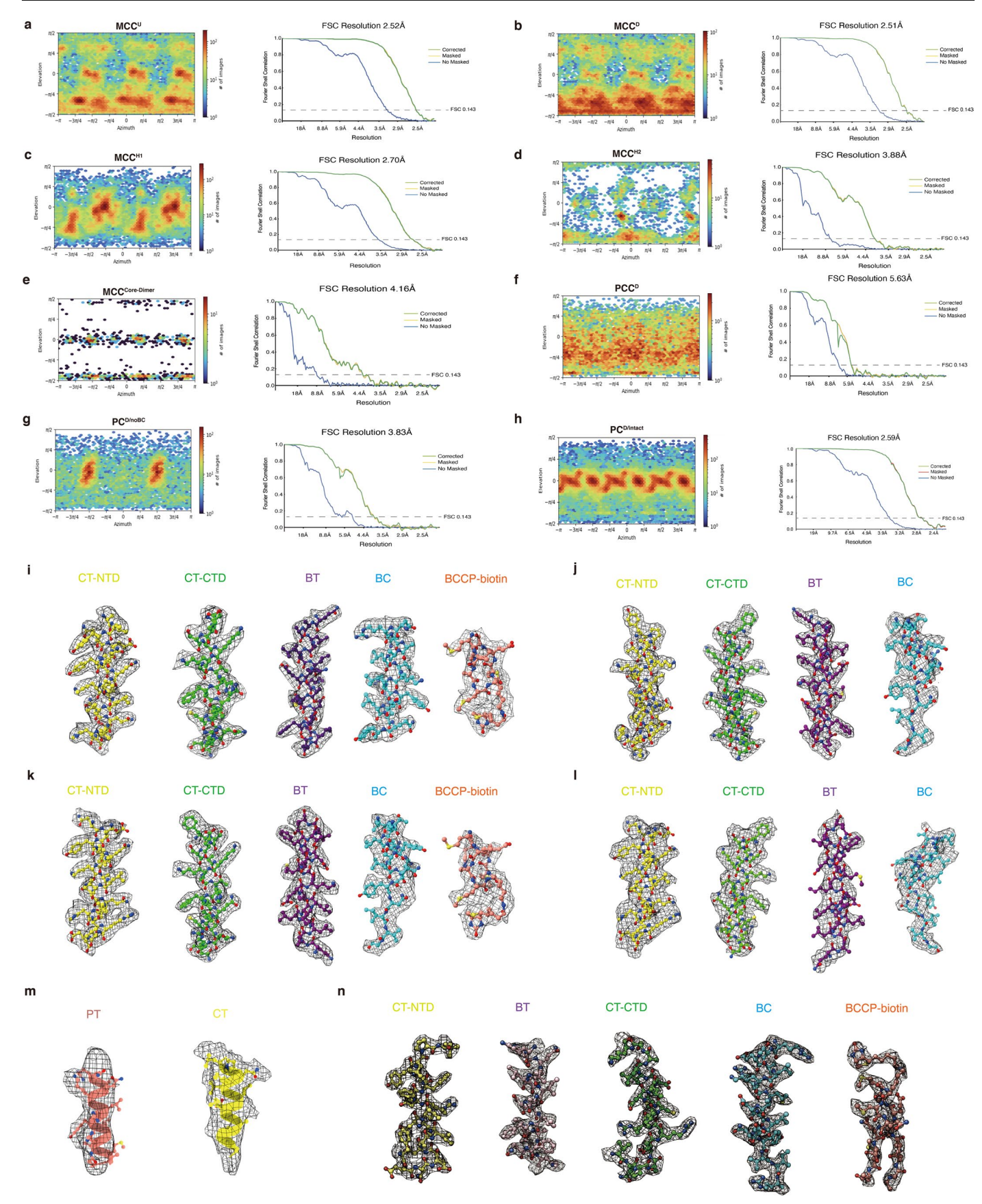
**Extended Data Fig. 1**| **Biochemical and Cryo-EM analysis result of the human MCC and PC complexes. (a)** Coomassie blue-stained SDS-PAGE of human MCC and PC complexes and Superose 6 profile of the affinity purified complexes. Each band in the red box was confirmed by mass spectrometry (Supplementary Table 1). Similar results were obtained for at least five times. **(b)** Coomassie blue-stained SDS-PAGE of cross-linked human MCC and PC complexes and Superose 6 profile of the cross-linked complexes. The bands of subunits present

in the uncross-linked sample (left panel of 1A) were disappeared, suggesting the formation of the cross-linked complex. Similar results were obtained for at least five times. (c) A representative raw micrograph containing MCC and PC complex from similar 1,245 micrographs and the power spectrum of the micrograph. (d) Summary of single-particle image analysis procedure of MCC and PC in cryoSPARC.



**Extended Data Fig. 2** | **Biochemical and Cryo-EM analysis result of the human PCC complex. (a)** Coomassie blue-stained SDS-PAGE of PCC complex and Superose 6 profile of the affinity purified human PCC complex. Each band in the red box was confirmed by mass spectrometry (Supplementary Table 2). Similar

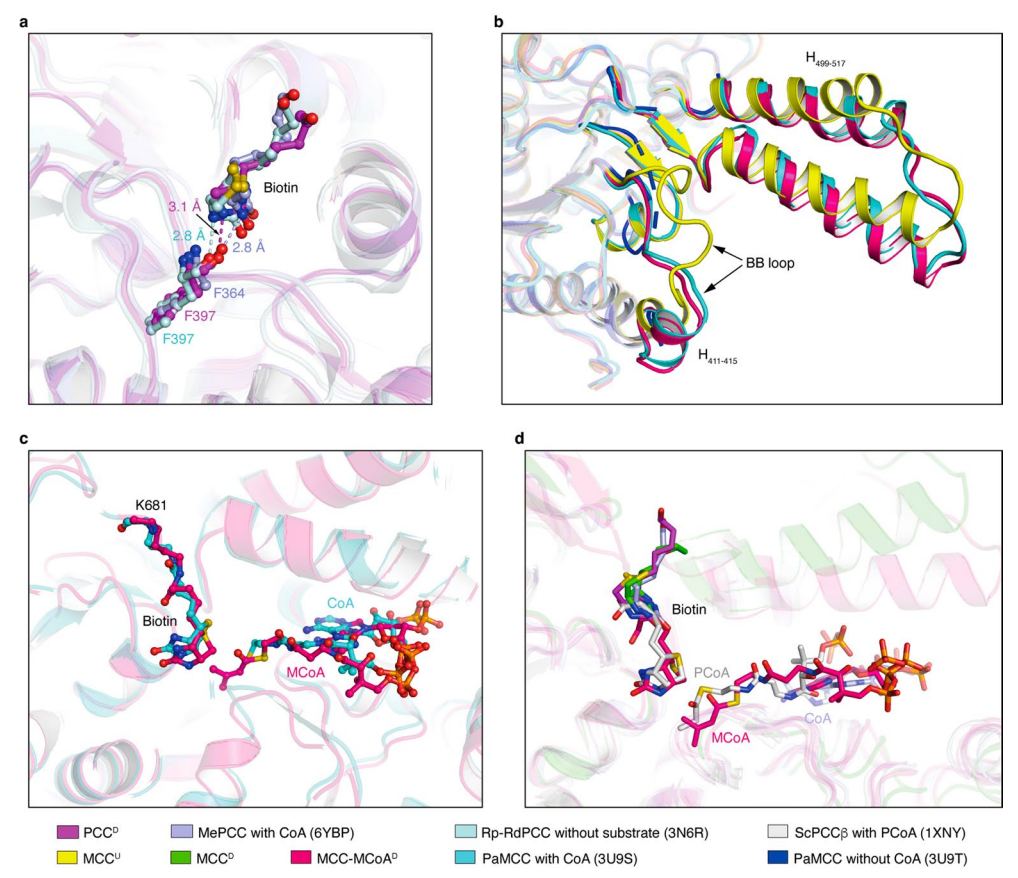
results were obtained for at least five times. **(b)** A representative raw micrograph containing PCC complex from similar 4,198 micrographs and the power spectrum of the micrograph. **(c)** Summary of single-particle image analysis procedure in cryoSPARC.



 $\textbf{Extended Data Fig. 3} \, | \, \textbf{See next page for caption.} \\$ 

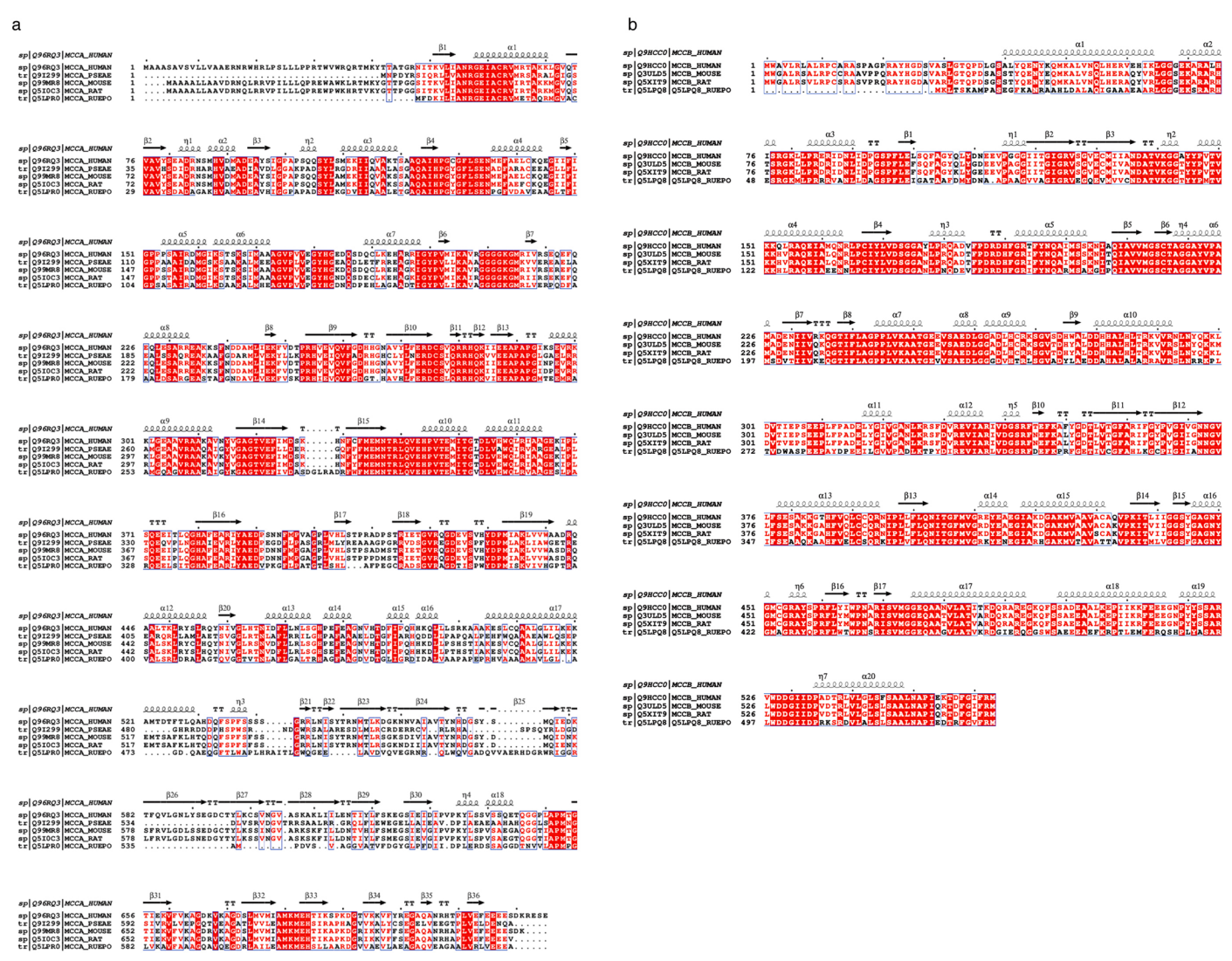
Extended Data Fig. 3 | Particle orientation distributions, FSC curves, and sample density maps. (a) Particle orientation distribution and FSC curve of  $MCC^U$  in cryoSPARC. (b) Particle orientation distribution and FSC curve of  $MCC^D$  in cryoSPARC. (c) Particle orientation distribution and FSC curve of  $MCC^{H1}$  in cryoSPARC. (d) Particle orientation distribution and FSC curve of  $MCC^{H2}$  in cryoSPARC. (e) Particle orientation distribution and FSC curve of Core-Dimer of

MCC (MCC<sup>Core-Dimer</sup>) in cryoSPARC. **(f)** Particle orientation distribution and FSC curve of PCC<sup>D</sup> in cryoSPARC. **(g)** Particle orientation distribution and FSC curve of PC<sup>D/noBC</sup> in cryoSPARC. **(h)** Particle orientation distribution and FSC curve of PC<sup>D/intact</sup> in cryoSPARC. **(i)** Sample maps of human MCC<sup>D</sup>. **(j)** Sample maps of human MCC<sup>U</sup>. **(k)** Sample maps of human MCC<sup>U</sup>. **(l)** Sample maps of human MCC<sup>U</sup>. **(m)** Sample maps of human PCC<sup>D</sup>. **(n)** Sample maps of human PCD<sup>D/noBC</sup>.

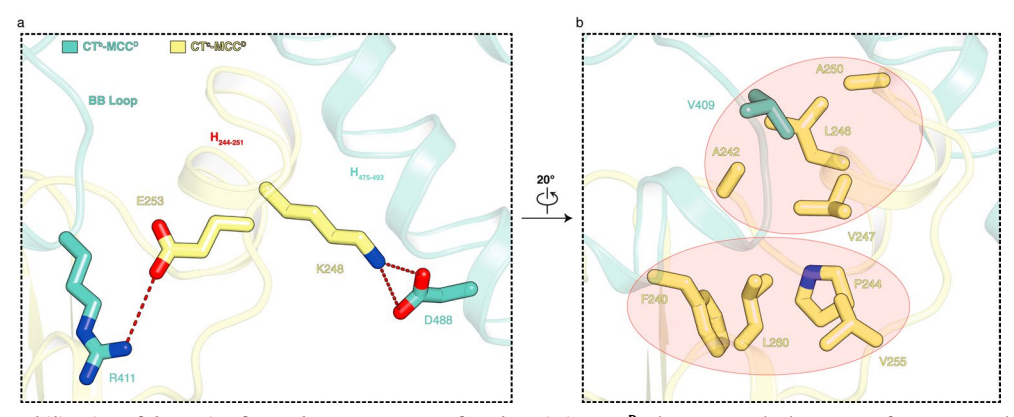


**Extended Data Fig. 4** | **Structural comparison of MCC and PCC from different species. (a)** Structural comparison of the biotin in the CT domain from human PCC<sup>D</sup>, MePCC-CoA complex (6YBP) and Rp-RdPCC without substrate (3N6R). **(b)** Structural comparison of human MCC<sup>U</sup>, human MCC-MCoA<sup>D</sup> and PaMCC-

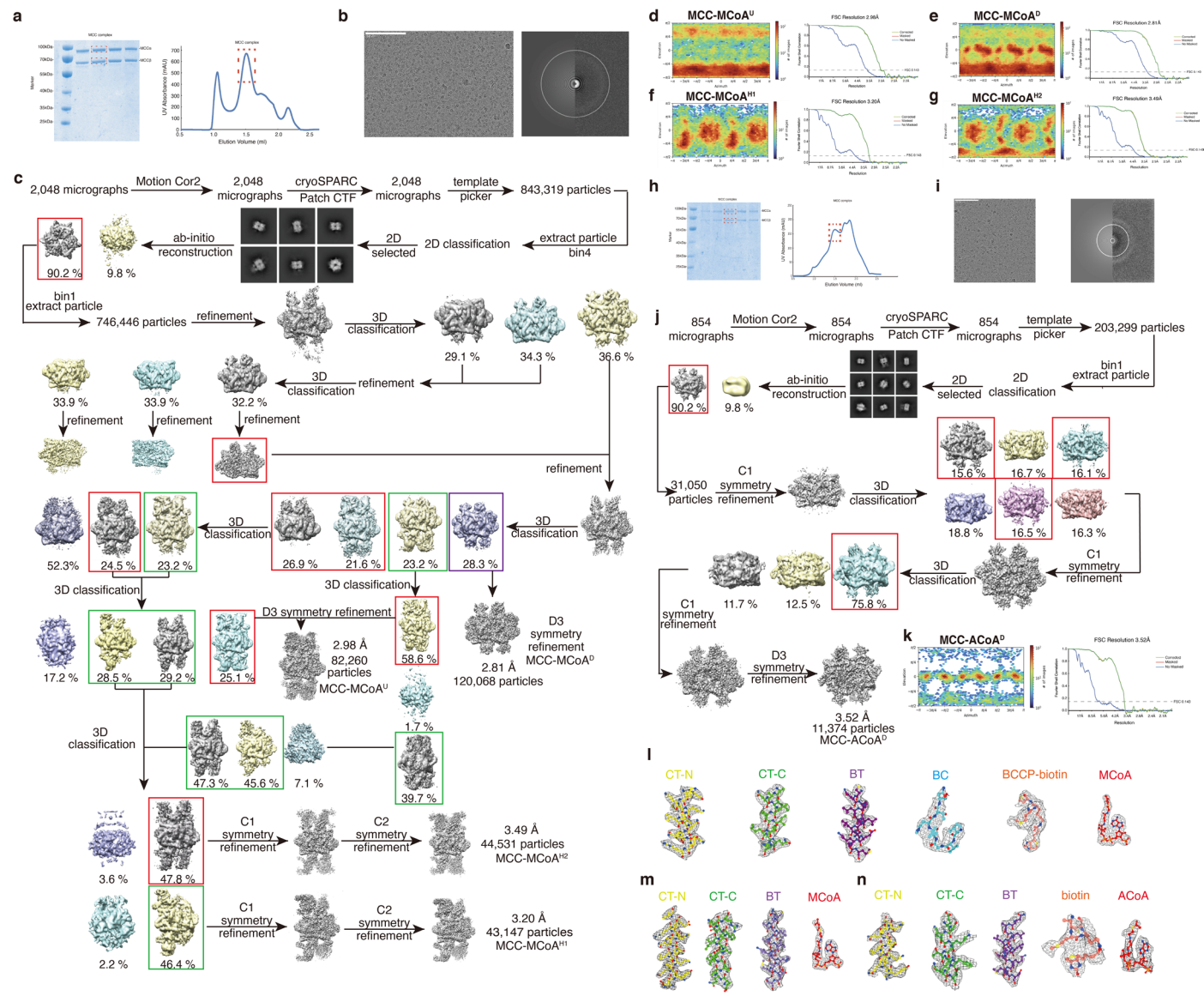
CoA (3U9S). (c) Structural comparison of human MCC-MCoA<sup>D</sup> and PaMCC-CoA (3U9S) to show the positions of biotin and substrates. (d) Structural comparison of human MCC<sup>D</sup>, human MCC-MCoA<sup>D</sup>, human PCC<sup>D</sup>, MePCC-CoA complex (6YBP) and ScPCC $\beta$ -PCoA complex (3N6R).



**Extended Data Fig. 5** | **Sequence alignment of MCC from different species.** (a) Sequence alignment of MCC $\alpha$  from different species. (b) Sequence alignment of MCC $\beta$  from different species.

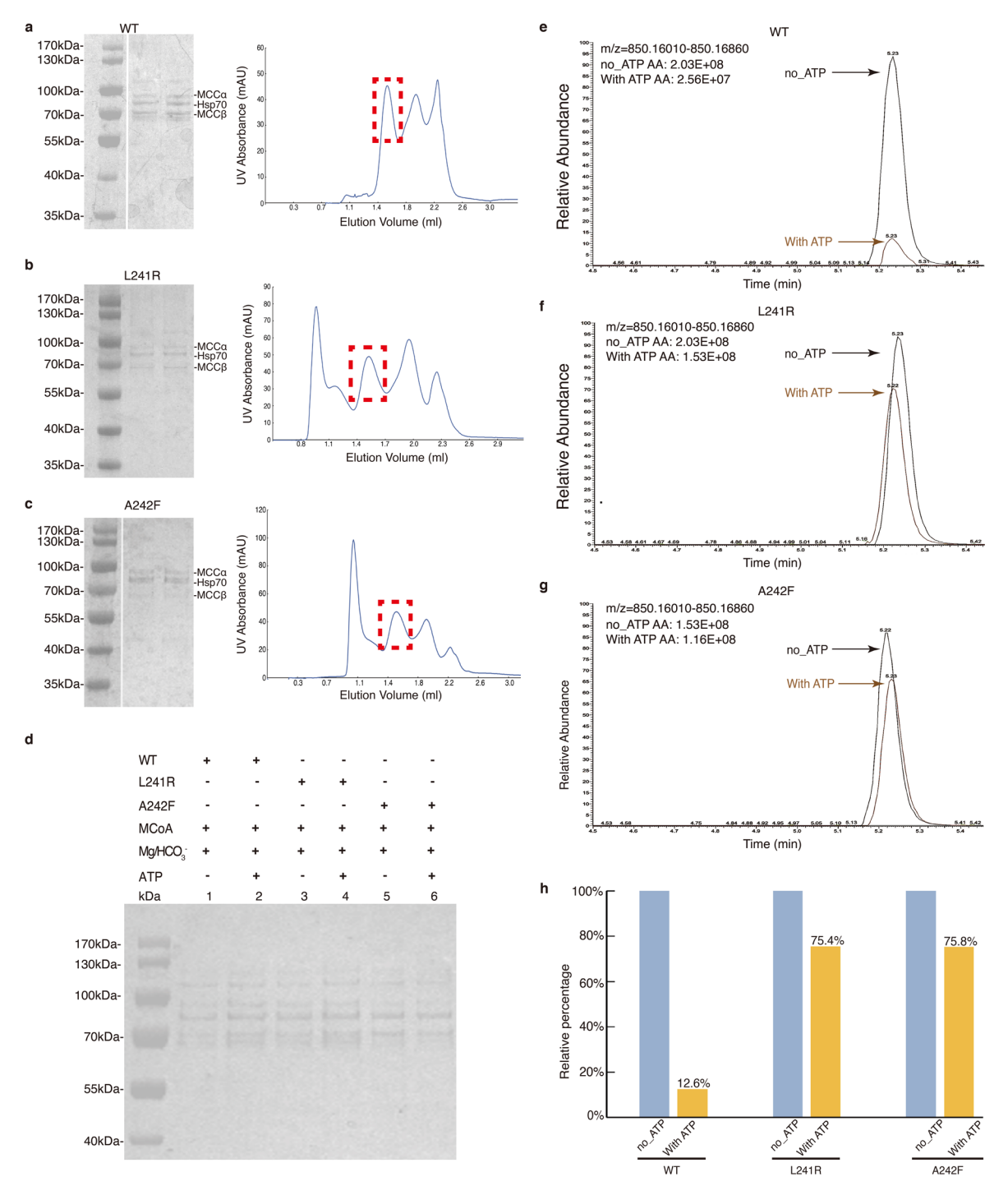


Extended Data Fig. 6 | Stabilization of the region from Ala242 to Leu260 of CT domain in MCC<sup>p</sup>. This region, which consists of two intermediate  $\alpha$ -helices (H<sub>244-251</sub> and H<sub>257-260</sub>) and the extended loops, is extensively contacted with surrounding residues through both electrostatic (a) and hydrophobic interactions (b).



Extended Data Fig. 7 | Biochemical and Cryo-EM analysis results of the MCoA-bound and ACoA bound MCC complexes. (a) Coomassie blue-stained SDS-PAGE of MCoA-bound MCC and Superose 6 profile of the affinity purified complex Similar results were obtained for two times. (b) A representative raw micrograph containing MCoA-bound MCC complex from similar 2,048 micrographs and the power spectrum of the micrograph. (c) Summary of single-particle image analysis procedure in cryoSPARC. (d) Particle orientation distribution and FSC curve between the EM map and the atomic model of the MCC-MCoA<sup>U</sup> with cryoSPARC. (e) Particle orientation distribution and FSC curve between the EM map and the atomic model of the MCC-MCoA<sup>D</sup> with cryoSPARC. (f) Particle orientation distribution and FSC curve between the EM map and the atomic

model of the MCC-MCoA<sup>HI</sup> with cryoSPARC. **(g)** Particle orientation distribution, local resolution map and FSC curve between the EM map and the atomic model of the MCC-MCoA<sup>HI</sup> with cryoSPARC. **(h)** Coomassie blue-stained SDS-PAGE of ACoA-bound MCC and Superose 6 profile of the affinity purified complex. Similar results were obtained for two times. **(i)** A representative raw micrograph containing ACoA-bound MCC complex from similar 854 micrographs and the power spectrum of the micrograph. **(j)** Summary of single-particle image analysis procedure in cryoSPARC. **(k)** Particle orientation distribution and FSC curve between the EM map and the atomic model of the MCC-ACoA<sup>D</sup> with cryoSPARC. **(l)** Sample maps of human MCC-MCoA<sup>U</sup>. **(m)** Sample maps of human MCC-MCoA<sup>D</sup>.



Extended Data Fig. 8 | Enzyme activity assays of wild-type and mutated MCC. (a-c) SDS-PAGE and FPLC curves of human wild-type (WT) MCC (a), mutant MCC L241R (b) and A242F (c). (d) The input of the enzyme activity assays. (e-g) LC-HRMS chromatograms of MCoA in the reaction with or without ATP for WT MCC

(e), mutant MCC L241R (f) and A242F (g). (H) The relative amount of MCoA. The amount of MCoA before the addition of ATP was arbitrarily defined as 100%. All experiments repeated two times.

# nature portfolio

| Corresponding author(s):   | Sen-Fang Sui |
|----------------------------|--------------|
| Last updated by author(s): | May 31, 2024 |

## **Reporting Summary**

Nature Portfolio wishes to improve the reproducibility of the work that we publish. This form provides structure for consistency and transparency in reporting. For further information on Nature Portfolio policies, see our <u>Editorial Policies</u> and the <u>Editorial Policy Checklist</u>.

For all statistical analyses, confirm that the following items are present in the figure legend, table legend, main text, or Methods section.

| _   |    |   |      |     |
|-----|----|---|------|-----|
| C - | トつ | 1 | ıctı | CC  |
| اد  | La | u | st   | いしろ |

| n/a             | Cor         | nfirmed  |
|-----------------|-------------|--|
|                 | $\boxtimes$ | The exact sample size $(n)$ for each experimental group/condition, given as a discrete number and unit of measurement  |
|                 | $\boxtimes$ | A statement on whether measurements were taken from distinct samples or whether the same sample was measured repeatedly  |
| $\boxtimes$     |             | The statistical test(s) used AND whether they are one- or two-sided Only common tests should be described solely by name; describe more complex techniques in the Methods section.   |
| $\boxtimes$     |             | A description of all covariates tested   |
| $\boxtimes$     |             | A description of any assumptions or corrections, such as tests of normality and adjustment for multiple comparisons  |
| $\boxtimes$     |             | A full description of the statistical parameters including central tendency (e.g. means) or other basic estimates (e.g. regression coefficient) AND variation (e.g. standard deviation) or associated estimates of uncertainty (e.g. confidence intervals) |
| $\boxtimes$     |             | For null hypothesis testing, the test statistic (e.g. <i>F</i> , <i>t</i> , <i>r</i> ) with confidence intervals, effect sizes, degrees of freedom and <i>P</i> value noted <i>Give P values as exact values whenever suitable.</i>                        |
| $\boxtimes$     |             | For Bayesian analysis, information on the choice of priors and Markov chain Monte Carlo settings   |
| $\boxtimes$     |             | For hierarchical and complex designs, identification of the appropriate level for tests and full reporting of outcomes   |
| $\boxtimes$     |             | Estimates of effect sizes (e.g. Cohen's d, Pearson's r), indicating how they were calculated   |
|                 |             | Our web collection on <u>statistics for biologists</u> contains articles on many of the points above.  |
| So <sup>-</sup> | ftw         | vare and code  |
| Poli            | y in        | formation about <u>availability of computer code</u>   |
| Da              | ita ci      | ollection AutoFMation  |

## For manuscripts utilizing custom algorithms or software that are central to the research but not yet described in published literature, software must be made available to editors and reviewers. We strongly encourage code deposition in a community repository (e.g. GitHub). See the Nature Portfolio guidelines for submitting code & software for further information.

CTFFIND4, MotionCor2 1.1.0, CryoSparc 3.3.1, Phenix 1.14-3260, Coot 0.8.9.1, PyMol 1.8.2.1, Chimera 1.12, ChimeraX 1.3, Xcalibur 4.2.47.

#### Data

Data analysis

Policy information about <u>availability of data</u>

All manuscripts must include a data availability statement. This statement should provide the following information, where applicable:

- Accession codes, unique identifiers, or web links for publicly available datasets
- A description of any restrictions on data availability
- For clinical datasets or third party data, please ensure that the statement adheres to our policy

The cryo-EM density map and atomic models have been deposited in the Electron Microscopy Data Bank and the Protein Data Bank. MCCU at 2.52 Å resolution (PDB: 8JAK, EMDB: 36128), MCCD at 2.51 Å resolution (PDB: 8JAW, EMDB: 36136), MCCH1 at 2.70 Å resolution (PDB: 8J7D, EMDB: 36038), MCCH2 at 3.88 Å resolution (PDB: 8J78, EMDB: 36034), MCCDore-Dimer at 4.16 Å resolution (PDB: 8J73, EMDB: 36024), PCD/noBC at 3.83 Å resolution (PDB: 8J70, EMDB: 36044), PCD/intact at 5.63 Å resolution (PDB: 8HWL, EMDB: 35059), PCCD at 2.59 Å resolution (PDB: 7YBU, EMDB: 33729), MCC-MCoAU at 2.98 Å resolution (PDB: 8JXL,

EMDB: 36704), MCC-MCoAD at 2.81 Å resolution (PDB: 8J4Z, EMDB: 35980), MCC-MCoAH1 at 3.20 Å resolution (PDB: 8JXN, EMDB: 36706), MCC-MCoAH2 at 3.49 Å resolution (PDB: 8JXM, EMDB: 36705), MCC-ACoAD at 3.52 Å resolution (PDB: 8K2V, EMDB: 36840). The publicly available structures used in this paper: PDB: 7WTA, 7WTC, 6YBP, 3N6R, 3U9S.

#### Research involving human participants, their data, or biological material

Policy information about studies with human participants or human data. See also policy information about sex, gender (identity/presentation), and sexual orientation and race, ethnicity and racism. Reporting on sex and gender N/A Reporting on race, ethnicity, or N/A other socially relevant groupings Population characteristics N/A N/A Recruitment Ethics oversight N/A Note that full information on the approval of the study protocol must also be provided in the manuscript. Field-specific reporting Please select the one below that is the best fit for your research. If you are not sure, read the appropriate sections before making your selection. X Life sciences Behavioural & social sciences Ecological, evolutionary & environmental sciences For a reference copy of the document with all sections, see <a href="mailto:nature.com/documents/nr-reporting-summary-flat.pdf">nature.com/documents/nr-reporting-summary-flat.pdf</a> Life sciences study design All studies must disclose on these points even when the disclosure is negative. Amount of single-paricle micrographs collected were based on the pre-experiments that reconstruction the protein particles on these Sample size micrographs could reach our expected resolution and also limited by the time allocation of the microscope. The exclusion criteria were not pre-established. 2D and 3D classification yielded multiple classes. Only the particles in the classes that showed Data exclusions clear structural signals and intact structures were selected, combined and used in the final reconstruction and refinement. Details are described in the flowchart of Extended Data Figure 1, Figure 2, Figure 6, and Methods. Replication The 2D and 3D classification repeated at least five times with slightly different parameters and local masks. The Refinements have been repeated at least five times with slightly different resolution. Protein purification by BAS and FPLC repeated five times with simialr results. The SDS page bands were analysed by MS twice. Gold standard Fourier Shell Correlation method was used to estimate the resolution of cryo-EM structures, in which the dataset is split into Randomization two set and refined independently. The process of splitting the dataset, odd and even, is considered random.

### Reporting for specific materials, systems and methods

Blinding

Blinding is not applicable to a cryo-EM experiments because no human research participants are involved.

We require information from authors about some types of materials, experimental systems and methods used in many studies. Here, indicate whether each material, system or method listed is relevant to your study. If you are not sure if a list item applies to your research, read the appropriate section before selecting a response.

| Materials & experimental systems                                     |                           | Methods   |  |  |  |
|--|---------------------------|---|--|--|--|
| n/a Involved in the study  |                           | n/a Involved in the study   |  |  |  |
| Antibodies   |                           | ChIP-seq  |  |  |  |
| Eukaryotic cell lines  |                           | Flow cytometry  |  |  |  |
| Palaeontology and a  | archaeology               | MRI-based neuroimaging  |  |  |  |
| Animals and other o  | organisms                 |   |  |  |  |
| Clinical data  |                           |   |  |  |  |
| Dual use research of   | f concern                 |   |  |  |  |
| Plants   |                           |   |  |  |  |
| 1  |                           |   |  |  |  |
| Eukaryotic cell lin  | es                        |   |  |  |  |
| Policy information about <u>ce</u>                                   |                           | and Gender in Research  |  |  |  |
|  |                           |   |  |  |  |
| Cell line source(s)  | HEK2931                   | cells were purchased from ThermoFisher Scientific (Cat#11625019).                                       |  |  |  |
| Authentication   | HEK293F                   | cells were directly purchased from ThermoFisher Scientifc and were not authenticated at out laboratory. |  |  |  |
| Mycoplasma contaminati   | on All cell li            | nes tested negative for mycoplasma contamination.   |  |  |  |
| Commonly misidentified lines (See ICLAC register)  No commonly misid |                           | nonly misidentified cell lines were used in this study.   |  |  |  |
| (  | (See <u>New</u> register) |   |  |  |  |
|  |                           |   |  |  |  |
| Plants   |                           |   |  |  |  |
| Seed stocks N/A  |                           |   |  |  |  |
|  | ,                         |   |  |  |  |
| Novel plant genotypes  | N/A                       |   |  |  |  |
|  |                           |   |  |  |  |
|  |                           |   |  |  |  |
| Authentication   | N/A                       |   |  |  |  |